JM PAPERS

On the inverse cascade and flow speed scaling behaviour in rapidly rotating Rayleigh–Bénard convection

S. Maffei[1,2,†], **M.J. Krouss**[1], **K. Julien**[3] **and M.A. Calkins**[1]

[1]Department of Physics, University of Colorado, Boulder, CO 80309, USA

[2]School of Earth and Environment, University of Leeds, Leeds LS2 9JT, UK

[3]Department of Applied Mathematics, University of Colorado, Boulder, CO 80309, USA

Rotating Rayleigh–Bénard convection is investigated numerically with the use of an asymptotic model that captures the rapidly rotating, small Ekman number limit, $Ek \to 0$. The Prandtl number (Pr) and the asymptotically scaled Rayleigh number ($\widetilde{Ra} = RaEk^{4/3}$, where Ra is the typical Rayleigh number) are varied systematically. For sufficiently vigorous convection, an inverse kinetic energy cascade leads to the formation of a pair of large-scale vortices of opposite polarity, in agreement with previous studies of rapidly rotating convection. With respect to the kinetic energy, we find a transition from convection dominated states to a state dominated by large-scale vortices at an asymptotically reduced (small-scale) Reynolds number of $\widetilde{Re} \approx 6$ ($\widetilde{Re} = ReEk^{1/3}$, where Re is the Reynolds number associated with vertical flows) for all investigated values of Pr. The ratio of the depth-averaged kinetic energy to the kinetic energy of the convection reaches a maximum at $\widetilde{Re} \approx 24$, then decreases as $\widetilde{Ra}$ is increased. This decrease in the relative kinetic energy of the large-scale vortices is associated with a decrease in the convective correlations with increasing Rayleigh number. The scaling behaviour of the convective flow speeds is studied; although a linear scaling of the form $\widetilde{Re} \sim \widetilde{Ra}/Pr$ is observed over a limited range in Rayleigh number and Prandtl number, a clear departure from this scaling is observed at the highest accessible values of $\widetilde{Ra}$. Calculation of the forces present in the governing equations shows that the ratio of the viscous force to the buoyancy force is an increasing function of $\widetilde{Ra}$, that approaches unity over the investigated range of parameters.

Key words: geostrophic turbulence, quasi-geostrophic flows, turbulent convection

† Email address for correspondence: s.maffei@leeds.ac.uk

S. Maffei, M.J. Krouss, K. Julien and M.A. Calkins

1. Introduction

Convection is common in the fluid regions of planets and stars. In particular, convection is the primary energy source for the generation of large-scale planetary and stellar magnetic fields (Jones 2011; Gastine *et al.* 2014; Aurnou *et al.* 2015), and it is thought to be a source of energy for the observed zonal flows in the atmospheres of the giant planets (e.g. Heimpel, Gastine & Wicht 2016). The flows in many of these natural systems are considered turbulent and strongly influenced by rotation; previous studies have shown that the combination of these physical ingredients can lead to an inverse kinetic energy cascade (e.g. Smith & Waleffe 1999; Seshasayanan & Alexakis 2018). The inverse cascade transfers kinetic energy from small-scale convection up to domain-scale flows, and, in a planar geometry of square cross-section, results in the formation of large-scale vortices (LSVs). (Julien *et al.* 2012*b*; Favier, Silvers & Proctor 2014; Guervilly, Hughes & Jones 2014; Rubio *et al.* 2014; Stellmach *et al.* 2014). Such vortices have a high degree of vertical invariance, tend to be characterised by flow speeds that are significantly larger than the underlying convection and can have an influence on heat transport and magnetic field generation (Guervilly *et al.* 2014; Guervilly, Hughes & Jones 2015). However, the convective vigour required to excite LSVs, how fluid properties (via the thermal Prandtl number) influence their formation and the scaling of their saturated amplitude with buoyancy forcing still remain poorly understood.

In planetary and astrophysical fluid systems, rapid rotation is thought to play an essential role in shaping the dynamics of convection. The importance of rotation for the dynamics of such systems is quantified by the Ekman and Rossby numbers, respectively defined as

$$Ek = \frac{\nu}{2\Omega H^2}, \quad Ro = \frac{U}{2\Omega H}, \tag{1.1a,b}$$

where ν is the kinematic viscosity, Ω is the rate of rotation, H is the spatial scale of the system (i.e. the depth of the fluid region) and U is a characteristic flow speed; Ek and Ro quantify, respectively, the ratio of viscous forces to the Coriolis force, and the ratio of inertia to the Coriolis force. Systems in which $(Ek, Ro) \ll 1$ are said to be rapidly rotating and rotationally constrained. For the Earth's outer core, for instance, estimates suggest that $Ek \simeq 10^{-15}$ and $Ro \simeq 10^{-5}$ (de Wijs *et al.* 1998; Rutter *et al.* 2002; Finlay & Amit 2011). It is currently impossible to use such extreme values of the governing parameters with direct numerical simulation (DNS). Quasi-geostrophic (QG) models have helped to overcome this deficiency, and have been critical for elucidating several convective phenomena that are thought to be of significant interest for planets, including identification of the primary flow regimes of rotating convection, heat transport behaviour and the convection-driven inverse cascade (Julien *et al.* 2012*b*; Rubio *et al.* 2014). QG models accurately capture the leading-order dynamics in systems characterised by small values of Ek and Ro.

Previous work has shown that the structure of LSVs is dependent on the relative importance of rotation: for sufficiently small values of Ek and Ro the large-scale structure is a pair of cyclonic and anticyclonic vortices (hereafter referred to as dipolar LSVs) with zero net (spatially averaged) vorticity (Julien *et al.* 2012*b*; Rubio *et al.* 2014; Stellmach *et al.* 2014); whereas for larger values of Ro the cyclonic vortex dominates over the anticyclonic one, leading to a net vorticity that is parallel to the rotation axis (Chan & Mayr 2013; Favier *et al.* 2014; Guervilly *et al.* 2014). QG models find only a pair of vortices of opposite polarity (dipolar LSVs), since they capture asymptotically small values of Ek and Ro only, in which there is no preferred sign for the vorticity. DNS studies have found dipolar LSVs when $Ek \approx 10^{-7}$ (Stellmach *et al.* 2014), and a dominantly cyclonic LSV when $Ek \gtrsim 10^{-6}$ (Chan & Mayr 2013; Favier *et al.* 2014; Guervilly *et al.* 2014).

This distinction in the LSV structure may have consequences on how heat transport and flow speeds are influenced by the inverse cascade. Moreover, for $Ro = O(1)$, the presence of a LSV appears to be dependent upon the initial condition used in the simulations (Favier, Guervilly & Knobloch 2019). In contrast, for the rapidly rotating regime studied here, we find that the formation of dipolar LSVs is not dependent upon initial conditions (see § 3.3 for details).

Natural systems are characterised by a broad range of fluid properties and, as a result, the Prandtl number $Pr = \nu/\kappa$ (where κ is the thermal diffusivity) can take on a wide range of values, ranging from $Pr = O(10^{-6})$ in stellar interiors (Ossendrijver 2003) to $Pr = O(10^{-2})$ for the liquid metals characteristic of planetary interiors (Pozzo *et al.* 2013). More generally, the density heterogeneities that lead to buoyancy-driven convection can also result from compositional differences, as is expected to be the case within terrestrial planetary interiors, for instance; under such circumstances the thermal Prandtl number in the governing equations is replaced by the compositional Schmidt number $Sc = \nu/D$, where D is a chemical diffusivity. For the Earth's outer core, studies suggest $Sc = O(100)$ for representative chemical species (e.g. Pozzo *et al.* 2013). This wide range of diffusivities that characterise geophysical and astrophysical fluids motivates the need for additional investigations that explore the influence of the Prandtl number on the dynamics, since all previous numerical calculations investigating the inverse cascade have focussed on fluids with $Pr = 1$. QG simulations (Julien *et al.* 2012*b*) have characterised the flow regimes that occur when $Pr \geqslant 1$. In general, it is found that low Pr fluids reach turbulent regimes for a lower value of the thermal forcing (as measured by the Rayleigh number Ra) than higher Pr fluids. More turbulent flows can be characterised by an increase in the Reynolds number

$$Re = UH/\nu, \tag{1.2}$$

which is a fundamental output parameter for convection studies. Many of the results found in QG studies have been confirmed by DNS calculations (Stellmach *et al.* 2014). In both approaches, the formation of LSVs has been tied to the geostrophic turbulence regime, which, prior to the present work, has not been observed for $Pr > 3$.

Laboratory experiments are an important tool for exploring the dynamics of rapidly rotating convection (e.g. Vorobieff & Ecke 2002; King *et al.* 2009; Kunnen, Geurts & Clercx 2010; Ecke & Niemela 2014; Stellmach *et al.* 2014) and, much like natural systems, can access a wide range of Pr values. Liquid metals ($Pr \approx 0.025$) (Aurnou & Olson 2001; Aubert *et al.* 2001; King & Aurnou 2013; Zimmerman *et al.* 2014; Adams *et al.* 2015; Aurnou *et al.* 2018; Vogt *et al.* 2018), water ($Pr \approx 7$) (Sumita & Olson 2002; Vorobieff & Ecke 2002; King *et al.* 2009; Cheng *et al.* 2015) and gases ($Pr \approx 1$) (Niemela, Babuin & Sreenivasan 2010; Ecke & Niemela 2014) have all been utilised. As for numerical calculations, fluids with smaller values of Pr reach higher values of Re than higher Pr fluids for equivalent Ra. From this perspective, such fluids are of significant interest for exploring the geostrophic turbulence regime of rapidly rotating convection (e.g. Julien *et al.* 2012*a*). However, the use of such low Pr fluids is not always practical and can reduce or eliminate flow visualisation opportunities. Furthermore, whereas small Pr fluids can lead to more turbulent flows, lower Ekman numbers must be used to provide a sufficiently large parameter regime over which the fluid remains rotationally constrained (e.g. King & Aurnou 2013). It would therefore be of use to identify the general dynamical requirements for observing inverse-cascade-generated LSVs for a variety of fluid properties.

One of the basic goals in convection studies is to determine the functional dependence of Re on the input parameters, namely, determination of the functional form $Re = f(Ra, Pr)$. Power-law scalings of the form $Re = c_1 Ra^{c_2} Pr^{c_3}$ are often sought, where each c_i is a constant. A well-known example is the so-called 'free-fall' scaling of the

form $Re \sim (Ra/Pr)^{1/2}$ observed in non-rotating convection (e.g. Ahlers, Grossmann & Lohse 2009; Orvedahl *et al.* 2018). The free-fall scaling arises from a balance between nonlinear advection and the buoyancy force in the momentum equation, and represents a 'diffusion-free' scaling in the sense that the flow speeds are independent of both the thermal and viscous diffusion coefficients. Motivated by this free-fall form of the scaling, and the assumption that natural systems are expected to be highly turbulent in the sense that $Re \gg 1$, rotating convection studies have also sought to find diffusion-free scalings for the flow speeds. For instance, the recent work of Guervilly, Cardin & Schaeffer (2019) observed $Re \sim RaEk/Pr$ in spherical convection simulations, which is also a diffusion-free scaling for the flow speeds. In the present work we show that this scaling is equivalent to $\widetilde{Re} \sim \widetilde{Ra}/Pr$, where $\widetilde{Re} = Ek^{1/3}Re$ and $\widetilde{Ra} = Ek^{4/3}Ra$ are, respectively, a Reynolds number and a Rayleigh based on the small convective scale ℓ. The $Re \sim RaEk/Pr$ scaling appears to be present for our larger Pr cases over a finite range in $\widetilde{Ra}$; as $\widetilde{Ra}$ is increased a significant departure in this scaling is observed.

In the present work we investigate the properties of the inverse cascade for varying $\widetilde{Ra}$ and Pr in the rapidly rotating asymptotic (QG) limit for thermal convection in a plane-layer geometry (rotating Rayleigh–Bénard convection). This choice allows for comparison with previous results from QG (Sprague *et al.* 2006; Julien *et al.* 2012*b*; Rubio *et al.* 2014) and DNS (Guervilly *et al.* 2014; Stellmach *et al.* 2014) plane-layer calculations. By exploring a parameter regime wider than previous studies we are able to characterise the formation of LSVs in greater detail. In particular, we derive a criterion, based on the ratio $\widetilde{Ra}/Pr$, that describes the transition to regimes where the barotropic energy is dominant over the wide range of Prandtl numbers considered here. Furthermore, we find evidence, for the first time to our knowledge, of very-high-$\widetilde{Re}$ regimes, previously unexplored, that show unexpected energetic and dynamic behaviours. The presence of these regimes prevents us from deriving scaling laws that are valid over the entire range of parameters considered here. The paper is organised as follows: in § 2 we describe the governing equations and diagnostic quantities; in § 3 the results of the simulations are presented and analysed; and a discussion is given in § 4.

2. Methodology

2.1. *Governing equations*

We consider rotating Rayleigh–Bénard convection in a plane-layer Cartesian geometry of depth H, with constant gravity vector $\boldsymbol{g} = -g\hat{\boldsymbol{z}}$ pointing vertically downward, perpendicular to the planar boundaries. The fluid is Boussinesq with thermal expansion coefficient α. The top boundary is held at constant temperature T_1 and the bottom boundary is held at constant temperature T_2 such that $\Delta T = T_2 - T_1 > 0$. The system rotates about the vertical with rotation vector $\boldsymbol{\Omega} = \Omega\hat{\boldsymbol{z}}$. In the limit of strong rotational constraint (i.e. small Rossby and Ekman numbers), the governing equations, can be reduced to the following set of equations (Julien *et al.* 2006; Sprague *et al.* 2006)

$$\partial_t \zeta + J[\psi, \zeta] - \partial_Z w = \nabla_\perp^2 \zeta, \tag{2.1}$$

$$\partial_t w + J[\psi, w] + \partial_Z \psi = \frac{\widetilde{Ra}}{Pr}\vartheta + \nabla_\perp^2 w, \tag{2.2}$$

$$\partial_t \vartheta + J[\psi, \vartheta] + w\partial_Z \bar{\Theta} = \frac{1}{Pr}\nabla_\perp^2 \vartheta, \tag{2.3}$$

$$\partial_Z(\overline{w\vartheta}) = \frac{1}{Pr}\partial_Z^2 \bar{\Theta}, \tag{2.4}$$

where ζ is the vertical component of the vorticity, ψ is the dynamic pressure and also the geostrophic streamfunction and w is the vertical component of the velocity. The vertical component of vorticity and the streamfunction are related via $\zeta = \nabla_\perp^2 \psi$, where $\nabla_\perp^2 = \partial_x^2 + \partial_y^2$. The non-dimensional temperature θ is decomposed into mean and fluctuating components $\bar{\Theta}$ and ϑ, respectively, such that $\theta = \bar{\Theta} + Ek^{1/3}\vartheta$. Here the mean is defined as an average over the small spatial (x, y, z) and the fast temporal (t) scales. The Jacobian operator $J[\psi, f] = \partial_x\psi\,\partial_y f - \partial_y\psi\,\partial_x f = \boldsymbol{u}_\perp \cdot \nabla_\perp f$ describes advection of the generic scalar field f by the horizontal velocity field $\boldsymbol{u}_\perp = (u, v, 0) = (-\partial_y\psi, \partial_x\psi, 0)$. The reduced Rayleigh number $\widetilde{Ra}$ is defined by

$$\widetilde{Ra} = Ek^{4/3}Ra, \tag{2.5}$$

where the standard Rayleigh number is

$$Ra = \frac{g\alpha\Delta T H^3}{\nu\kappa}. \tag{2.6}$$

Equations (2.1)–(2.4) have been non-dimensionalised by the small-scale viscous diffusion time ℓ^2/ν, where the small horizontal convective length scale is $\ell = HEk^{1/3}$. The derivation of the reduced system relies on the assumption that the Coriolis force and pressure gradient force are balanced at leading order, i.e. geostrophic with $\hat{\boldsymbol{z}} \times \boldsymbol{u} = -\nabla_\perp\psi$. This force balance implies the Taylor–Proudman constraint is satisfied on small vertical scales such that $\partial_z(\boldsymbol{u}, \psi) = 0$ (e.g. Stewartson & Cheng 1979). Therefore, along the vertical direction all fluid variables vary on an $O(H)$ dimensional scale associated with the coordinate $Z = Ek^{1/3}z$. As a result, fast inertial waves with dimensional frequency $O(\Omega)$ are filtered from the above equations, allowing for substantial computational savings. However, slow, geostrophically balanced inertial waves are retained (Julien *et al.* 2012*b*).

The mean temperature $\bar{\Theta}$ evolves on the slow time scale $\tau = Ek^{2/3}t$ associated with the vertical diffusion time H^2/ν. However, Julien, Knobloch & Werne (1998) and Plumley *et al.* (2018) found that spatial averaging over a sufficient number of convective elements on the small scales is sufficiently accurate to (i) omit fast-time averaging and (ii) assume a statistically stationary state where the slow evolution term $\partial_\tau\bar{\Theta}$ that would appear in (2.4) is omitted.

Finally, we note that three-dimensional incompressibility is invoked through the solenoidal condition for the ageostrophic, sub-dominant horizontal velocity,

$$\nabla_\perp \cdot \boldsymbol{u}_\perp^{ag} + \partial_Z w = 0, \tag{2.7}$$

where $\boldsymbol{u}_\perp^{ag} = O(Ek^{1/3}\boldsymbol{u}_\perp)$.

The equations are solved using impenetrable, stress-free mechanical boundary conditions, and constant temperature boundary conditions. However, it should be noted that the specific form of the thermal boundary conditions is unimportant in the limit of rapid rotation (Calkins *et al.* 2015), and the present model can be generalised to no-slip mechanical boundary conditions (Julien *et al.* 2016). Each variable is represented with a spectral expansion consisting of Chebyshev polynomials in the vertical (Z) dimension, and Fourier series in the horizontal (x, y) dimensions. The resulting set of equations are truncated and solved numerically with a pseudo-spectral algorithm that uses a third-order implicit/explicit Runge–Kutta time-stepping scheme (Spalart, Moser & Rogers 1991). The code has been benchmarked successfully and used in many previous investigations (Marti, Calkins & Julien 2016; Maffei *et al.* 2019; Yan *et al.* 2019).

Spatial and temporal resolutions of the simulations performed for this study are given in table 1. The horizontal dimensions of the domain are periodic and scaled by the critical horizontal wavelength $\lambda_c = 2\pi/k_c \approx 4.8154$, measured in small-scale units ℓ. Most of the simulations use horizontal dimensions of $10\lambda_c \times 10\lambda_c$, although some additional simulations with different domain sizes were also carried out to quantify the influence of the geometry. We find that a domain size of $10\lambda_c \times 10\lambda_c$ is sufficient for accurate computation of statistical quantities, though the role of LSVs appears to become increasingly important with increasing domain size; we discuss this effect in our results.

2.2. *Depth-averaged dynamics and energetics*

For the purpose of investigating the inverse energy cascade, we decompose the vertical vorticity into a depth-averaged (barotropic) component, $\langle \zeta \rangle$, and a fluctuating (baroclinic) component, ζ', such that

$$\zeta = \langle \zeta \rangle + \zeta', \tag{2.8}$$

where, by definition, $\langle \zeta' \rangle = 0$. The depth-averaged (barotropic) vorticity equation is then found by vertically averaging equation (2.1), and is given by

$$\partial_t \langle \zeta \rangle + J[\langle \psi \rangle, \langle \zeta \rangle] = -\langle J[\psi', \zeta'] \rangle + \nabla_\perp^2 \langle \zeta \rangle. \tag{2.9}$$

Thus, the barotropic dynamics are governed by a two-dimensional vorticity equation in which the sole forcing comes from the convective dynamics, represented by the first term on the right-hand side of the above equation.

The barotropic, time-dependent kinetic energy density is defined as follows:

$$K_{bt}(t) = \tfrac{1}{2}\left(\overline{\langle u \rangle^2 + \langle v \rangle^2}^{\mathcal{V}} \right) = \tfrac{1}{2}\overline{|\nabla_\perp \langle \psi \rangle|^2}^{\mathcal{V}}, \tag{2.10}$$

where $\overline{\cdot}^{\mathcal{V}}$ indicates an average over the small, horizontal spatial scales, consistent with the notation employed in Plumley *et al.* (2018). In Fourier space, the barotropic kinetic energy equation is derived by multiplying the Fourier representation of (2.9) by the complex conjugate of $-\langle \psi \rangle_{\boldsymbol{k}} \exp(\mathrm{i}\boldsymbol{k} \cdot \boldsymbol{x})$, the spectral representation of $\langle \psi \rangle$, and integrating over physical space to obtain

$$\partial_t K_{bt}(k) = T_k + F_k + D_k, \tag{2.11}$$

where the box-normalised horizontal wavenumber vector is $\boldsymbol{k} = (k_x, k_y, 0)$, and $k = |\boldsymbol{k}|$. This equation describes the evolution of the kinetic energy contained in the barotropic mode of wavenumber k that is due to (i) the interaction with the other barotropic modes,

$$T_k = \sum_{|\boldsymbol{k}|=k} Re\{\langle \psi \rangle_{\boldsymbol{k}}^* \circ \mathcal{F}_{\boldsymbol{k}}[J[\langle \psi \rangle, \langle \zeta \rangle]]\}; \tag{2.12}$$

(ii) the interaction with the baroclinic, convective modes,

$$F_k = \sum_{|\boldsymbol{k}|=k} Re\{\langle \psi \rangle_{\boldsymbol{k}}^* \circ \mathcal{F}_{\boldsymbol{k}}[\langle J[\psi', \zeta'] \rangle]\}; \tag{2.13}$$

and (iii) the viscous dissipation of the barotropic mode,

$$D_k = \sum_{|\boldsymbol{k}|=k} Re\{|\boldsymbol{k}|^2 \langle \psi \rangle_{\boldsymbol{k}}^* \circ \langle \zeta \rangle_{\boldsymbol{k}}\}. \tag{2.14}$$

In the above definitions, the superscript $*$ denotes a complex conjugate, $\mathcal{F}_{\boldsymbol{k}}[\cdot]$ indicates the horizontal Fourier transform of the argument in square brackets, the symbol $\circ$ indicates a

913 A18-6

Hadamard (element-wise) product, $Re\{\cdot\}$ is the real part of the argument in curly brackets and the sum is taken over all horizontal wavenumbers. The barotropic-to-barotropic and baroclinic-to-barotropic transfer functions T_k and F_k can be explicitly expressed in terms of a triadic interaction due to the Jacobian (i.e. nonlinear) terms (Rubio *et al.* 2014). The formation of LSVs is due to a positive contribution from T_k and F_k in (2.11) at the domain-scale wavenumber $k = 1$. As LSVs form, the kinetic energy grows in time until dissipation balances the positive transfer at $k = 1$. Eventually, a statistically stationary state is reached where $\bar{D}_k \approx -(\bar{T}_k + \bar{F}_k)$, where we notice that, for these quantities, $\bar{\cdot}$ is equivalent to an average over the fast temporal scale only; in contrast with previous work, all of the simulations presented here have reached this stationary state. Hereafter, in order to simplify notation we omit the averaging operator and refer only to the time-averaged values of K_{bt}, T_k, F_k and D_k, unless otherwise stated.

2.3. *Diagnostic quantities*

Here, we define several diagnostic quantities that will be used to characterise the dynamical state of the convective system. The heat transfer across the fluid layer is quantified by the non-dimensional Nusselt number

$$Nu = 1 + Pr\overline{\langle w\theta \rangle}. \tag{2.15}$$

In the present study the small-scale, or convective, Reynolds number is defined as characterising

$$\widetilde{Re} = \frac{\langle W_{rms} \rangle \ell}{\nu} = \langle w_{rms} \rangle, \tag{2.16}$$

where $W_{rms} = (\bar{W}^2)^{1/2}$ and $w_{rms} = (\bar{W}^2)^{1/2}$ are the root-mean-square (r.m.s.) values of the dimensional and non-dimensional vertical velocity component, respectively. The above definition is particularly useful for characterising the amplitude of the convective motions, rather than the large-amplitude horizontal motions that occur in the presence of a strong inverse cascade. We also find it useful to refer to instantaneous values of the Nusselt and Reynolds number, and denote these by $Nu(t)$ and $\widetilde{Re}(t)$, respectively.

Together with the barotropic kinetic energy (2.10) we will also consider the time-averaged baroclinic, vertical and total kinetic energy densities, respectively defined as

$$K_{bc} = \tfrac{1}{2}\overline{\langle (u')^2 + (v)'^2 \rangle} = \tfrac{1}{2}\langle |\nabla_\perp \psi'|^2 \rangle; \tag{2.17}$$

$$K_z = \tfrac{1}{2}\langle \bar{w}^2 \rangle, \tag{2.18}$$

$$K = \tfrac{1}{2}\overline{\langle u^2 + v^2 + w^2 \rangle} = \tfrac{1}{2}\langle |\nabla_\perp \psi|^2 \rangle + K_z. \tag{2.19}$$

With the above definitions, the Reynolds number can be expressed as $\widetilde{Re} = \sqrt{2K_z}$. As for Nu and $\widetilde{Re}$, we find it useful to refer to the instantaneous values of the total kinetic energy density as $K(t)$.

2.4. *Domain of validity of the QG equations and comparison with DNS*

The asymptotic equations (2.1)–(2.4) are valid for low Rossby number convection only; this constraint implies that $\widetilde{Ra} \leqslant O(Ek^{-1/3})$ and $Pr \geqslant O(Ek^{1/4})$ (Julien *et al.* 2012b). The violation of these conditions signifies the weakening of the dominant geostrophic balance

and a loss of rotational constraint. As a relevant natural example, for the Earth's outer core these conditions are $\widetilde{Ra} \leqslant O(10^5)$ and $Pr \geqslant O(10^{-3.75})$. The former is most likely satisfied, although large uncertainties remain concerning the estimation of $\widetilde{Ra}$ for the core (see Cheng *et al.* (2015) for a discussion); the latter is satisfied since $Pr = O(10^{-2})$ for liquid metals. For recent DNS, for which $Ek = O(10^{-7})$ (Stellmach *et al.* 2014), the rapidly rotating regime is bounded by $\widetilde{Ra} \leqslant O(10^{2.5})$ and $Pr \geqslant O(10^{-1.75})$; although the latter is typically satisfied since $Pr = O(1)$ in numerical studies, the former is within reach in the present study. Note that the $\widetilde{Ra} \leqslant O(Ek^{-1/3})$ constraint does not limit the QG equation to low-Ra regimes. However, it does limit the range of Ra for which the QG approximation is valid given the Ek of the unscaled convective system. The smaller the Ek of the unscaled system, the larger the range of Ra for which the convective flows can be considered rotationally constrained, and for which the reduced equations (2.1)–(2.4) can be used (King, Stellmach & Aurnou 2012; Gastine, Wicht & Aubert 2016; Plumley & Julien 2019). As $\widetilde{Ra} \gtrsim O(Ek^{-1/3})$ the physical system under consideration should be studied with DNS, since the QG model only captures rotationally constrained dynamics.

The asymptotic model (2.1)–(2.4) has been tested against stress-free DNS calculations in rapidly rotating regimes satisfying the above bounds, with excellent agreement between the two approaches (Stellmach *et al.* 2014). The effect of no-slip boundaries can be included in the asymptotic equations (2.1)–(2.4) by parametrising the effect of the Ekman layers on the interior flow (Julien *et al.* 2016). Results from the asymptotic equations can then be compared with no-slip DNS and laboratory experiments, again with excellent agreement (Plumley *et al.* 2016). In particular, heat transport data (*Nu*) were successfully compared with DNS with $Ek = 10^{-7}$ and $1 \leqslant Pr \leqslant 7$ (Stellmach *et al.* 2014; Plumley *et al.* 2016), and with laboratory experiments with water (Cheng *et al.* 2015), for $2 \times 10^{-8} \lesssim Ek \lesssim 3 \times 10^{-6}$ (Plumley *et al.* 2016). Furthermore, the same morphological differences in the flow regimes obtained with increasing $\widetilde{Ra}$ (see Sprague *et al.* (2006), Julien *et al.* (2012*b*), Cheng *et al.* (2015) and § 3) were found in both numerical (DNS and asymptotic) and laboratory experiments. Of particular interest to the present study, LSV formation has been observed in both DNS and asymptotic calculations for $Pr = 1$ (Sprague *et al.* 2006; Julien *et al.* 2012*b*; Favier *et al.* 2014; Guervilly *et al.* 2014; Rubio *et al.* 2014; Stellmach *et al.* 2014), for $\widetilde{Ra} \gtrsim 3\widetilde{Ra}_c$, where $\widetilde{Ra}_c$ is the critical value for the onset of thermal convection. However, as mentioned in § 1, the LSVs in DNS are predominantly cyclonic due to a local reduction of the rotational constraint in the anticyclonic component (Guervilly *et al.* 2014). On the contrary, the LSVs in QG calculations are always dipolar in structure due to the limit of asymptotically small of Ro. This is guaranteed by a known reflection symmetry in this limit (Hakim, Snyder & Muraki 2002; Sprague *et al.* 2006). Furthermore, as the thermal driving is increased and the condition $\widetilde{Ra} \leqslant O(Ek^{-1/3})$ is violated, the system transitions towards three-dimensional, isotropic turbulence and LSV formation is gradually lost in DNS (Guervilly *et al.* 2014). This transition also makes subcritical sustenance of the LSVs possible (Favier *et al.* 2019): an artificially injected, highly energetic, cyclonic LSV is stable in the transition regimes for which domain-scale, barotropic vortices would not spontaneously form. This rich phenomenology is characteristic of regimes for which $\widetilde{Ra} \gtrsim O(Ek^{-1/3})$ in which $Ro = O(1)$ and so it is not observed in QG simulations, for which Ro and Ek are asymptotically small and the leading-order geostrophic balance is explicitly enforced. Therefore, no LSV subcritical behaviour is observed in asymptotic calculations (see § 3.3), and no upper limit to $\widetilde{Ra}$ for LSV formation can be achieved as a consequence of the loss of rotational constraint.

3. Results

3.1. *Flow morphology: two-scale flows*

The details of the simulations performed for this study are given in table 1. The choice of parameters allows us to refine the results of previous QG calculations (Julien *et al.* 2012*b*) in the range $1 \leqslant Pr \leqslant 3$ and for $Pr = 7$, of particular relevance for laboratory experiments. The temporally averaged values of $\widetilde{Re}$ and Nu displayed in table 1 are calculated over a temporal window in which the system reached a statistically stationary state. If LSVs are present in the domain, $\widetilde{Re}$ and Nu might reach stationary values only when the barotropic kinetic energy has saturated, in accordance with previous studies (Julien *et al.* 2012*b*; Favier *et al.* 2014; Guervilly *et al.* 2014; Rubio *et al.* 2014) where Nu has been shown to evolve over the time needed for the total kinetic energy to saturate. The interested reader is directed to supplementary figure 1 available at https://doi.org/10.1017/jfm.2020.1058 for an example of this behaviour. Figures 1(*a*) and 1(*c*) shows $\widetilde{Re}$ and Nu as functions of $\widetilde{Ra}$ and Pr. The continuous lines in figure 1(*a*) indicate the least-square fit to a power law of the kind $\widetilde{Re} = \alpha_r (\widetilde{Ra} - \widetilde{Ra}_c)^{\beta_r} Pr^{\gamma_r}$ with $\alpha_r = 0.1883$, $\beta_r = 1.1512$ and $\gamma_r = -1.2172$. In figure 1(*b*) we illustrate the collapse of the $\widetilde{Re}$ data points to the law $\widetilde{Re} \sim (\widetilde{Ra} - \widetilde{Ra}_c) Pr^{-1}$, empirically found and consistent with the coefficients β_r and γ_r. Figure 1(*b*) suggests that the reduced Grashof number, $\widetilde{Ra} Pr^{-1}$ plays a key role in controlling the dynamics. Figure 1(*d*) shows the collapse of the Nu data points to a power law of the kind $Nu \sim (\widetilde{Ra} - \widetilde{Ra}_c)^{3/2} Pr^{-1/2}$, distinctive of the ultimate regime of thermal convection. Inspection of figures 1(*c*) and 1(*d*) reveals the complex nature of the scaling behaviour of Nu with respect to the input parameters, in agreement with previous studies (Julien *et al.* 2012*b*). In particular we note that the Pr-dependence does not trivially separate the original data when displayed as a function of $\widetilde{Ra}$ (as opposed as to the $\widetilde{Re}$ data in figure 1*a*). Further details concerning power-law fits are given in § 3.5.

Following Julien *et al.* (2012*b*), inspection of volumetric renderings of the fluctuating temperature (figure 2) suggests that we can qualitatively classify the flows into: the cellular regime (*C*); the convective Taylor column regime (CTC); the plume regime (*P*); and the geostrophic turbulence regime (*G*). Regime *C* is only obtained close to the onset of thermal convection, i.e. for Rayleigh numbers not much larger than the critical value of $\widetilde{Ra}_c \simeq 8.7$; the CTC regime is characterised by columns that stretch across the fluid layer, surrounded by 'sleeves' of oppositely signed vorticity (also visible in the fluctuating temperature) that prevent columns from interacting with each other; in the *P* regime the insulation mechanism weakens and column–column interaction shortens these structures, transforming them into plumes; finally, geostrophic turbulence prevails at sufficiently large Rayleigh numbers where no obvious coherence in the fluctuating temperature field is observed. Although distinct transitions in the flow statistics can sometimes be used to separate these flow regimes (Nieves, Rubio & Julien 2014), an obvious distinction cannot always be made, e.g. cases ($\widetilde{Ra} = 40$, $Pr = 2$) and ($\widetilde{Ra} = 60$, $Pr = 3$) shown in figure 2, where plumes generated at each horizontal boundary seem to coexist with columns spanning the whole vertical extension of the computational domain.

For a given value of Pr, we observe the formation of LSVs as $\widetilde{Ra}$ is increased. These dipolar LSVs are readily identified from visual inspection of the geostrophic streamfunction ψ. Some representative cases are shown in figure 3. Crucially, we observe LSV formation for all Pr values reported in table 1, including, for the first time to our knowledge, $Pr > 3$. We find that for the LSVs to be present in the domain, convection does not need to be in the geostrophic turbulent regime, as was previously suggested (Julien *et al.* 2012*b*; Stellmach *et al.* 2014).

Pr	$\widetilde{Ra}$	$N_x \times N_y \times N_z$	Δt	$\widetilde{Re} \pm \sigma_{\widetilde{Re}}$	$Nu \pm \sigma_{Nu}$
1	20	$128 \times 128 \times 64$	5×10^{-3}	3.5408 ± 0.0860	4.010 ± 0.130
1	30	$128 \times 128 \times 64$	5×10^{-4}	7.2190 ± 0.1805	7.9603 ± 0.3688
1	40	$256 \times 256 \times 64$	5×10^{-4}	10.586 ± 0.307	11.788 ± 0.569
1	60	$256 \times 256 \times 96$	1×10^{-4}	16.822 ± 0.558	19.961 ± 0.953
1	80	$384 \times 384 \times 128$	5×10^{-5}	24.685 ± 0.711	30.92 ± 1.25
1	120	$384 \times 384 \times 192$	5×10^{-5}	41.40 ± 2.59	58.20 ± 4.32
1	160	$256 \times 256 \times 256$	1×10^{-4}	59.4 ± 12.4	98.06 ± 9.95
1	200	$384 \times 384 \times 384$	5×10^{-5}	84.21 ± 6.76	146.24 ± 12.38
1.5	20	$128 \times 128 \times 96$	1×10^{-3}	2.2527 ± 0.0482	3.990 ± 0.108
1.5	30	$128 \times 128 \times 96$	1×10^{-3}	4.366 ± 0.103	8.075 ± 0.315
1.5	40	$192 \times 192 \times 122$	5×10^{-4}	6.7529 ± 0.227	12.439 ± 0.584
1.5*	50*	$164 \times 164 \times 108$	5×10^{-4}	9.082 ± 0.239	16.348 ± 0.758
1.5	60	$192 \times 192 \times 136$	5×10^{-4}	11.0592 ± 0.434	20.39 ± 1.01
1.5	80	$244 \times 244 \times 136$	1×10^{-4}	14.772 ± 0.506	28.51 ± 0.999
1.5	120	$256 \times 256 \times 256$	1×10^{-4}	23.899 ± 0.881	49.11 ± 2.32
1.5	160	$256 \times 256 \times 256$	1×10^{-4}	35.39 ± 2.30	75.37 ± 4.76
2	20	$128 \times 128 \times 72$	1×10^{-3}	1.6744 ± 0.0442	4.0143 ± 0.0852
2	40	$192 \times 192 \times 122$	5×10^{-4}	4.9194 ± 0.0965	13.149 ± 0.427
2*	45*	$192 \times 192 \times 128$	1×10^{-4}	5.812 ± 0.124	15.142 ± 0.525
2	50	$192 \times 192 \times 128$	1×10^{-4}	6.803 ± 0.164	17.749 ± 0.674
2	60	$192 \times 192 \times 136$	1×10^{-4}	8.361 ± 0.171	21.39 ± 1.05
2	80	$192 \times 192 \times 136$	1×10^{-4}	11.342 ± 0.413	29.56 ± 1.28
2	120	$404 \times 404 \times 256$	1×10^{-4}	17.186 ± 0.531	46.74 ± 1.96
2	160	$224 \times 224 \times 256$	1×10^{-4}	23.57 ± 1.52	66.38 ± 2.81
2	200	$256 \times 256 \times 256$	1×10^{-4}	30.4862 ± 1.66	93.80 ± 4.14
2.5	20	$128 \times 128 \times 72$	1×10^{-3}	1.3277 ± 0.0276	3.994 ± 0.108
2.5	40	$192 \times 192 \times 122$	5×10^{-4}	3.8869 ± 0.0903	13.863 ± 0.665
2.5*	55*	$216 \times 216 \times 128$	1×10^{-4}	6.067 ± 0.134	21.286 ± 0.850
2.5*	60*	$216 \times 216 \times 128$	5×10^{-4}	6.837 ± 0.168	23.50 ± 1.01
2.5	80	$216 \times 216 \times 136$	1×10^{-4}	9.364 ± 0.236	31.75 ± 1.31
2.5	160	$216 \times 216 \times 256$	1×10^{-4}	19.55 ± 1.35	68.3 ± 3.39
2.5	200	$256 \times 256 \times 256$	1×10^{-4}	24.7205 ± 1.55	91.00 ± 5.42
3	50	$288 \times 288 \times 128$	5×10^{-4}	4.290 ± 0.106	19.402 ± 0.770
3*	60*	$192 \times 192 \times 128$	1×10^{-4}	5.551 ± 0.139	24.853 ± 0.943
3	70	$512 \times 512 \times 128$	1×10^{-4}	6.919 ± 0.155	30.14 ± 1.26
3*	80*	$256 \times 256 \times 128$	1×10^{-4}	8.060 ± 0.184	34.27 ± 1.58
3	120	$216 \times 216 \times 186$	1×10^{-4}	11.226 ± 0.246	50.24 ± 1.55
7	20	$(512 \times 512 \times 32)^{\dagger}$	1×10^{-2}	0.45662 ± 0.00387	4.0696 ± 0.0369
7	40	$256 \times 256 \times 32$	1×10^{-3}	1.3293 ± 0.0179	14.761 ± 0.119
7	60	$256 \times 256 \times 64$	1×10^{-3}	2.4907 ± 0.0522	32.86 ± 1.42
7	80	$256 \times 256 \times 64$	2×10^{-4}	3.5423 ± 0.0792	44.73 ± 1.55
7	100	$384 \times 384 \times 92$	2×10^{-4}	4.748 ± 0.108	62.39 ± 2.37
7	120	$384 \times 384 \times 92$	2×10^{-4}	5.831 ± 0.122	74.46 ± 2.67
7	135	$384 \times 384 \times 92$	1×10^{-4}	6.150 ± 0.133	82.32 ± 2.80
7	160	$512 \times 512 \times 92$	1×10^{-4}	7.448 ± 0.138	92.51 ± 2.51

Table 1. For caption see on next page.

Table 1 (cntd). Details of the numerical simulations: Pr is the Prandtl number; $\widetilde{Ra}$ is the reduced Rayleigh number; N_x, N_y and N_Z are, respectively, the number of Fourier modes in the x and y directions and the number of Chebyshev modes in the Z direction; Δt is the time-step size used during the simulation; $\widetilde{Re} = \langle w_{rms} \rangle$ is the time-averaged, reduced Reynolds number based on the vertical component of the velocity; Nu is the time-averaged Nusselt number; $\sigma_{\widetilde{Re}}$ and σ_{Nu} are the standard deviations of $\widetilde{Re}$ and Nu, respectively. The superscript † indicates that the horizontal box size for the simulation is taken to be $20\lambda_c \times 20\lambda_c$, where $\lambda_c = 2\pi/k_c$ is the critical wavelength for the onset of thermal convection; for all other cases the box size is $10\lambda_c \times 10\lambda_c$. The superscript ∗ indicates cases for which the influence of the lack or presence of LSVs in the initial condition on the saturated state has been checked (see § 3.3 for details).

3.2. *LSV characterisation*

To quantify the presence of LSVs in the domain we analysed the time-averaged barotropic kinetic energy spectra $K_{bt}(k)$. We define flows in which LSVs are energetically dominant by the two conditions: $K_{bt} > K_{bc}$; and $K_{bt}(k = 1) \geqslant K_{bt}(k > 1)$. As examples, figure 4(*a,b*) shows the barotropic kinetic energy spectra for $Pr = 1$ and $Pr = 2$ over a range in $\widetilde{Ra}$. The transition to LSV-dominant states occurs within the ranges $20 < \widetilde{Ra} < 30$ and $40 < \widetilde{Ra} < 45$ for the $Pr = 1$ and the $Pr = 2$ cases, respectively. As $\widetilde{Ra}$ is further increased beyond the transition, LSVs becomes increasingly dominant, as shown by progressively larger values of $K_{bt}(k)$ for $k < 3$. Note that for the ($\widetilde{Ra} = 20$, $Pr = 1$) case, the barotropic spectra has a maximum at $k = 1$. However, for this case, the barotropic kinetic energy is not dominant, rather, we find that $K_{bc} \simeq 3K_{bt}$ for this case. Therefore, there are no energetically dominant LSVs in the domain for this particular case.

Figure 4(*a,b*) suggests that the spectral slope at low wavenumbers saturates at the behaviour $K_{bt}(k) \sim k^{-4}$ for fully developed LSVs. This suggestion can be corroborated by inspection of the compensated spectra $k^4 K_{bt}(k)$, shown in figure 4(*c,d*). Note that, while the $Pr = 2$ cases do suggest a saturation of the low-k spectral slope to a $K_{bt}(k) \sim k^{-4}$ law, the $Pr = 1$ show a steeper slope (specifically between $k^{-4.2}$ and $k^{-4.3}$) for $\widetilde{Ra} = 200$. Whether this is a sign that the saturation slope is Pr-dependent or that the $Pr = 1$ cases have not yet reached the saturation regime, lies beyond the scope of the present work. The scaling $K_{bt}(k) \sim k^{-3}$, associated with the presence of LSVs in rapidly rotating thermal convection studies (Julien *et al.* 2012*b*; Rubio *et al.* 2014), two-dimensional (Smith & Yakhot 1993, 1994; Borue 1994; Chertkov *et al.* 2007) and rotating three-dimensional (Smith & Waleffe 1999) turbulence studies, is shown for comparison. Some low-*Ro* calculations in triply periodic domains with a barotropic driving force (Seshasayanan & Alexakis 2018) also suggest a low-k spectral slope steeper than k^{-3}. However, given the different nature of the driving force and boundary conditions it is not straightforward to relate this previous work with the present results. Indeed, it has been shown in triply periodic simulations of synthetically forced, rotating turbulence, that the details of the imposed forcing (e.g. spatial scales, isotropy, net helicity) has profound consequences on the development of the inverse energy cascade and on the low-k slope of the saturated energy spectra (Sen *et al.* 2012; Pouquet *et al.* 2013).

The phenomenology described above for $Pr = 1$ and $Pr = 2$ is observed for all Pr considered in the present study, although the threshold Rayleigh number for LSV-dominant state increases with Pr. However, we observe that the LSVs become energetically dominant provided $\widetilde{Re} \gtrsim 6$, independent of Pr. The lowest value for which LSV formation has been observed is $\widetilde{Re} = 5.812$ for the ($\widetilde{Ra} = 45, Pr = 2$) case. We indicate this value
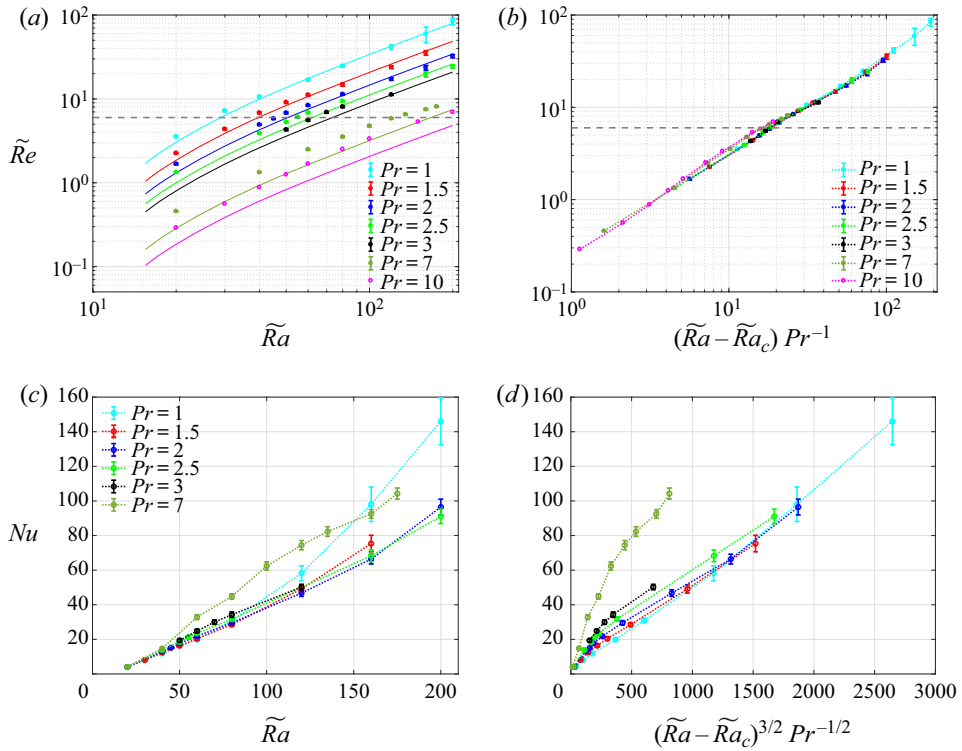
Figure 1. (*a*,*b*) Temporally averaged Reynolds number $\widetilde{Re}$ and (*c*,*d*) Nusselt number Nu for all of the simulations: (*a*) $\widetilde{Re}$ versus the reduced Rayleigh number $\widetilde{Ra}$; (*b*) $\widetilde{Re}$ versus the rescaled quantity $(\widetilde{Ra} - \widetilde{Ra}_c)/Pr$; (*c*) Nu versus $\widetilde{Ra}$; (*d*) Nu versus the rescaled coordinate $(\widetilde{Ra} - \widetilde{Ra}_c)^{3/2}Pr^{-1/2}$. Continuous lines in (*a*) show the best-fit, three parameter power-law scaling $\widetilde{Re} = \alpha_r(\widetilde{Ra} - \widetilde{Ra}_c)^{\beta_r}Pr^{\gamma_r}$, where $\alpha_r = 0.1883$, $\beta_r = 1.1512$ and $\gamma_r = -1.2172$ (see § 3.5). Data for $Pr = 10$ in (*a*,*b*) are from Calkins *et al.* (2016). The dashed horizontal lines in (*a*,*b*) show the Reynolds number at which the box-scale depth-averaged kinetic energy becomes dominant (see § 3.2).

by the horizontal dashed line in figures 1(*a*) and 1(*b*). The only exception is the $(\widetilde{Ra} = 55, Pr = 2.5)$ case for which no energetically dominant LSVs are observed, although $\widetilde{Re} = 6.067 \pm 0.134$. This discrepancy can be explained by noting that these two values of $\widetilde{Re}$ are (considering their temporal fluctuations) consistent with each other and by admitting that the transition to LSV-dominated regime is not abrupt. A more detailed exploration of the parameter space around the transition could reveal other exceptions to the threshold we identified and possibly a subtle Pr dependence.

In addition to the transition shown in the barotropic kinetic energy spectra, we also find (with increasing $\widetilde{Ra}$) a distinct transition in the character of the three terms present in the spectral kinetic energy equation (2.11). In figure 4(*e*,*f*) we illustrate how the time-averaged, barotropic energy transfer $T_k + F_k$ evolves with $\widetilde{Ra}$ for the specific case of $Pr = 2$. We note that $[T_k + F_k]_{k=1} > 0$ for all of the cases investigated, indicating that energy is always being transferred to the $k = 1$ mode, regardless of the value of $\widetilde{Ra}$. However, we find that $T_k + F_k$ changes from possessing a peak at $k > 1$, to then peaking at $k = 1$ for a sufficiently large value of $\widetilde{Ra}$; for the $Pr = 2$ data shown this transition occurs when $\widetilde{Ra} > 50$. Analysing all of our simulations shows that this transition occurs when $\widetilde{Re} \geqslant 6.491$, for any value of Pr. This threshold value corresponds to the simulation $(\widetilde{Ra} = 135, Pr = 7)$ and it is noted that no simulation with $\widetilde{Re} < 6.491$ satisfies
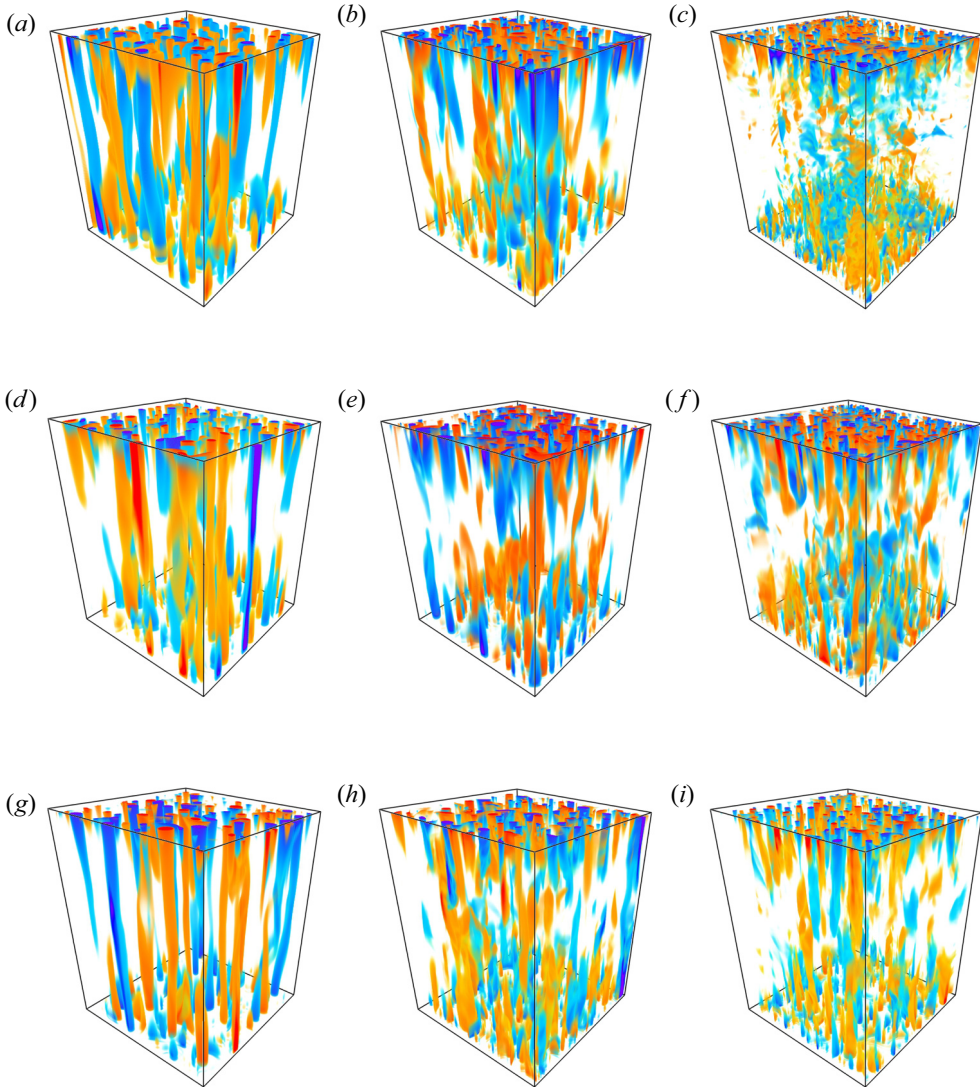
913 A18-12

Figure 2. Volumetric renderings of fluctuating temperature, ϑ, showing the different convective regimes for increasing Rayleigh number (left to right) and increasing Prandtl number (top to bottom). The abbreviations correspond to: convective Taylor column (CTC); plume (P); geostrophic turbulence (G). See online supplementary material for movies illustrating the temporal evolution of the fluctuating temperature for selected values of $\widetilde{Ra}$ and Pr: (a) $\widetilde{Ra} = 40, Pr = 2$ (CTC/P); (b) $\widetilde{Ra} = 60, Pr = 2$ (P); (c) $\widetilde{Ra} = 200, Pr = 2$ (G); (d) $\widetilde{Ra} = 60, Pr = 3$ (CTC/P); (e) $\widetilde{Ra} = 80, Pr = 3$ (P); (f) $\widetilde{Ra} = 120, Pr = 3$ (P); (g) $\widetilde{Ra} = 80, Pr = 7$ (CTC); (h) $\widetilde{Ra} = 135, Pr = 7$ (P); (i) $\widetilde{Ra} = 160, Pr = 7$ (P).

$[T_k + F_k]_{k=1} > [T_k + F_k]_{k>1}$. The only exception is the case $(\widetilde{Ra} = 40, Pr = 1.5)$, for which $\widetilde{Re} = 6.7529 \pm 0.227$ and the energy transfer at $k = 1$ is subdominant. Again, given the finite fluctuations in the $\widetilde{Re}$ values, we argue that a transition region may exist for which a simple threshold rule may not always work; a more detailed exploration of the parameter space may reveal subtle Pr dependencies in the transition into the regime for which the barotropic energy transfer at $k = 1$ is dominant.
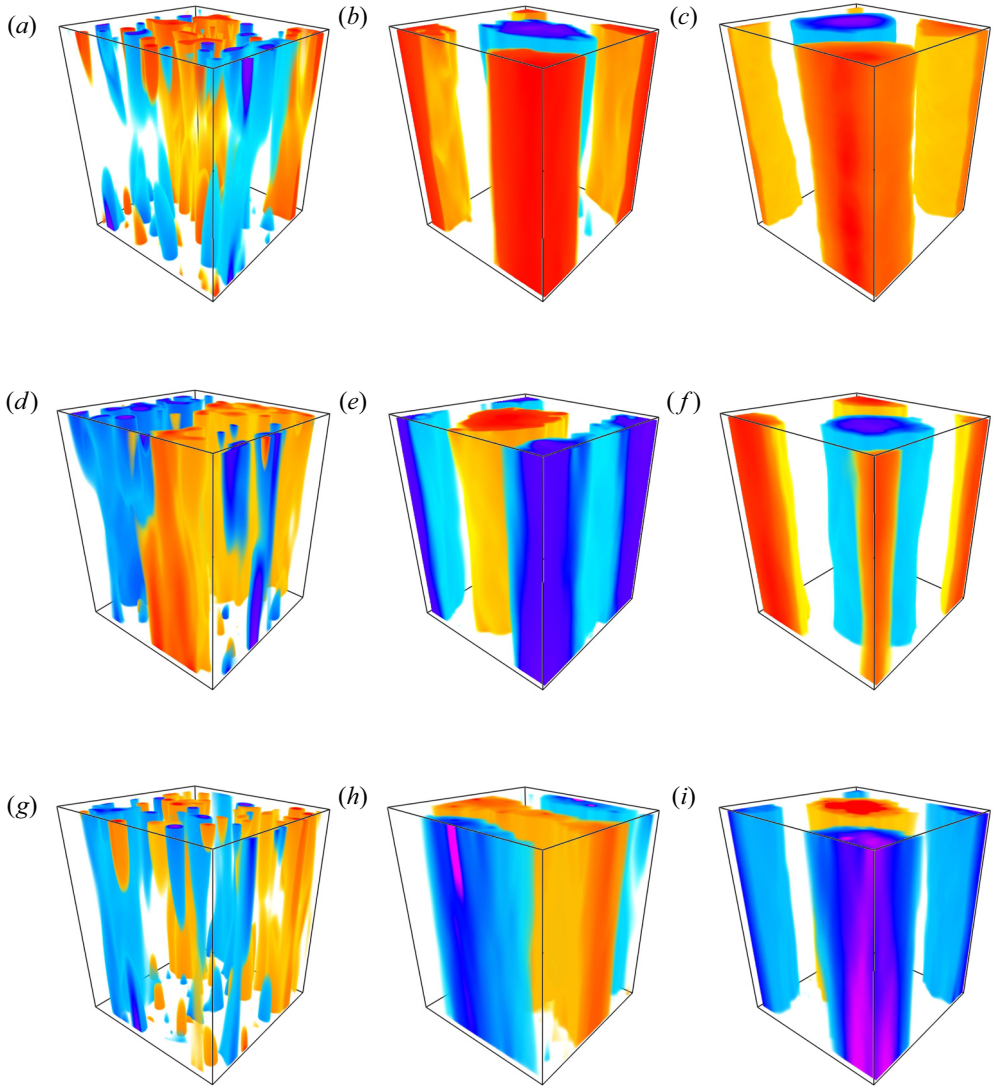
Figure 3. Volumetric renderings of the geostrophic streamfunction (pressure), ψ, showing the development of large-scale vortices (LSVs) for increasing Rayleigh number (left to right) and increasing Prandtl number (top to bottom): (*a*) $\widetilde{Ra} = 40, Pr = 2$; (*b*) $\widetilde{Ra} = 60, Pr = 2$; (*c*) $\widetilde{Ra} = 200, Pr = 2$; (*d*) $\widetilde{Ra} = 60, Pr = 3$; (*e*) $\widetilde{Ra} = 80, Pr = 3$; (*f*) $\widetilde{Ra} = 120, Pr = 3$; (*g*) $\widetilde{Ra} = 80, Pr = 7$; (*h*) $\widetilde{Ra} = 135, Pr = 7$; (*i*) $\widetilde{Ra} = 160, Pr = 7$.

Closer inspection of F_k and T_k separately (figure 4*f*) indicates that the baroclinic, convective dynamics primarily transfers energy to the barotropic dynamics around $k \simeq 5$ (notice the positive peak in F_k for $k \simeq 5$). Energy transferred to the barotropic dynamics is then transferred upscale by the barotropic nonlinear interactions, as indicated by negative values of T_k for wavenumbers $k > 4$, and positive values at the largest scales. The inverse cascade that leads to LSV formation is therefore directly driven by the barotropic nonlinear interactions in (2.9), whereas the energy is provided by the interaction of the baroclinic dynamics with the barotropic flows. The fact that $\sum_{k \geqslant 0} T_k = 0$ confirms that the nonlinear barotropic interactions do not inject or extract barotropic energy and that the saturation of

913 A18-14
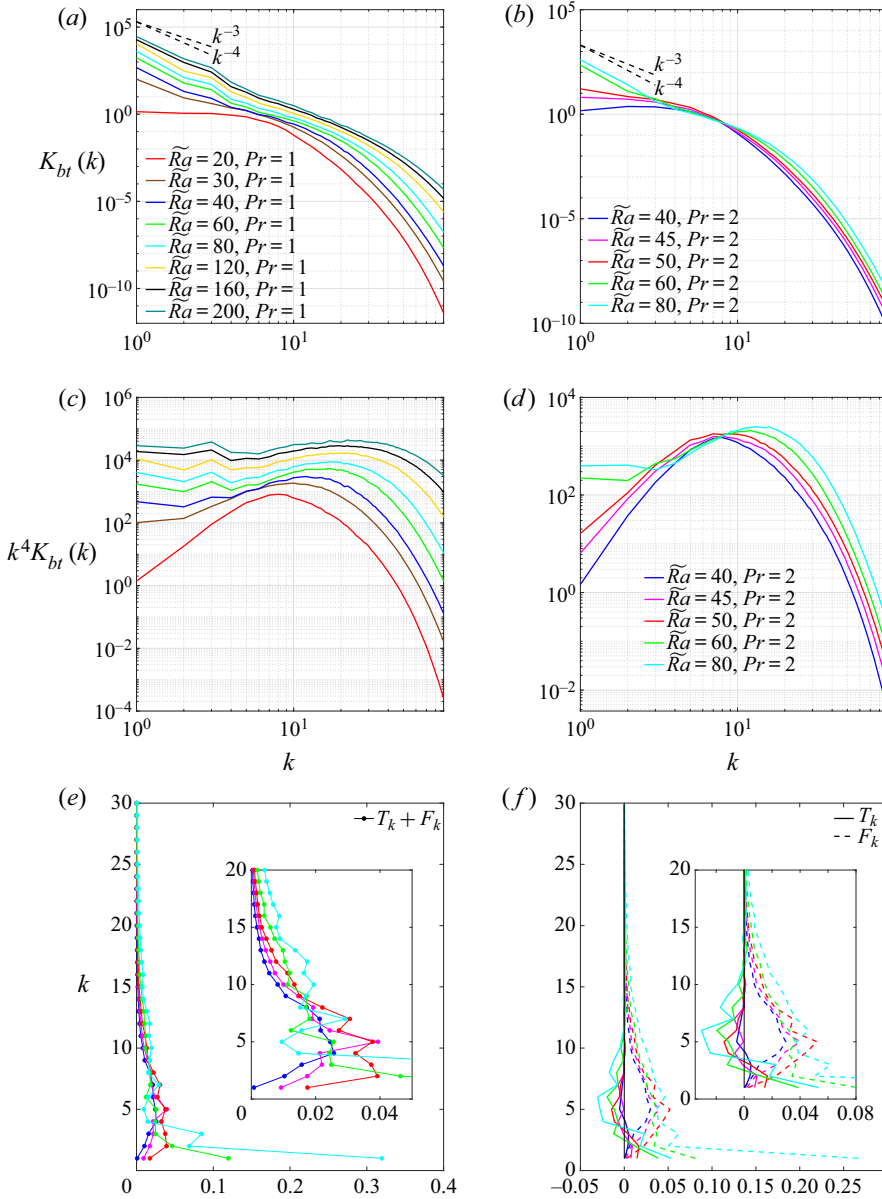
Figure 4. (*a*,*b*) Spectra of the barotropic kinetic energy $K_{bt}(k)$ for select values of $\widetilde{Ra}$ and for $Pr = 1$ and $Pr = 2$. The scalings $K_{bt}(k) \sim k^{-3}$ and $K_{bt}(k) \sim k^{-4}$ are shown for comparison. (*c*,*d*) Compensated spectra $k^4 K_{bt}(k)$ for the same cases shown in (*a*,*b*). (*e*) Barotropic transfer $T_k + F_k$ for the $Pr = 2$ cases; (*f*) barotropic-to-barotropic (T_k) and baroclinic-to-barotropic (F_k) for the $Pr = 2$ case separately illustrated in continuous and dashed lines, respectively. Colour legend for (*e*,*f*) is the same as in (*b*,*d*). A black vertical line is drawn in correspondence of $T_k, F_k = 0$. The insets highlight the behaviour for $\widetilde{Ra} \leqslant 50$. All quantities have been time averaged over a statistically stationary state for which $T_k + F_k \approx -D_k$.

K_{bt} is controlled by the balance between energy injected from the baroclinic dynamics and energy dissipated through viscosity

$$0 \approx \sum_{k \geqslant 0} F_k + \sum_{k \geqslant 0} D_k. \tag{3.1}$$

913 A18-15
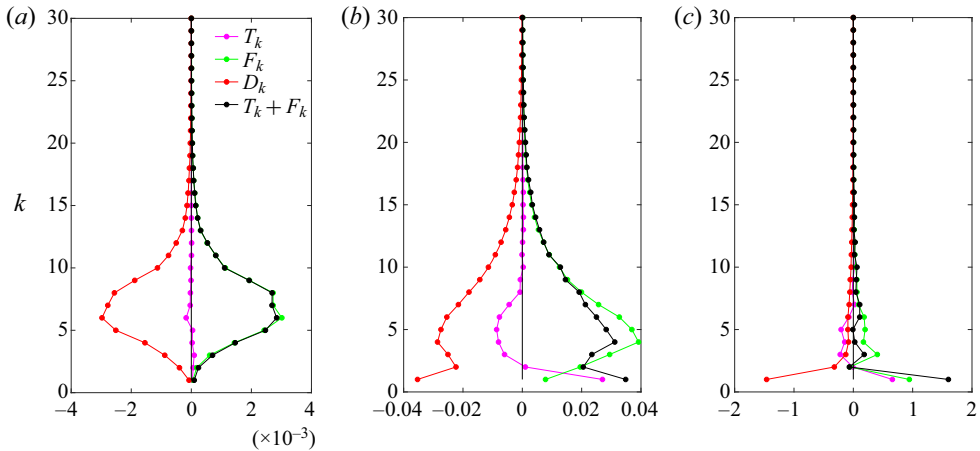
Figure 5. Time-averaged, barotropic transfer functions showing the change in energy transfer behaviour as the inverse cascade becomes more prominent. All cases use $\widetilde{Ra} = 60$ and Prandtl numbers (a) $Pr = 7$ ($\widetilde{Re} \approx 2.5$), (b) $Pr = 2.5$ ($\widetilde{Re} \approx 6.8$) and (c) $Pr = 1$ ($\widetilde{Re} \approx 16.8$). These three cases are representative of, respectively, the CTC/P regime, showing no LSVs in the domain and $\widetilde{Re} \ll 6$; the P regime, showing LSVs in the domain and $\widetilde{Re} \gtrsim 6$; the G regime, with robust LSVs and $\widetilde{Re} \gg 6$.

This mechanism is in agreement with the formation of large-scale condensates in two-dimensional (2-D) calculations (Borue 1994; Smith & Yakhot 1994; Chertkov *et al.* 2007; Laurie *et al.* 2014) where the transfer of energy is due to the nonlinear interactions between different scales of the 2-D flow (equivalent to the barotropic-to-barotropic energy transfer described by T_k). This view is also confirmed by recent 3-D studies (Buzzicotti *et al.* 2018).

As mentioned in § 2.2, in the saturated state $D_k \approx -(T_k + F_k)$. Examples are shown in figure 5 for $\widetilde{Ra} = 60$ and $Pr = 7$, $Pr = 2.5$ and $Pr = 1$. These cases are representative of, respectively, a low-turbulence case at the edge of the CTC and P regimes where $\widetilde{Re} \ll 6$ and, consequently, an inverse cascade that is not strong enough to drive LSV formation; a case in the P regime with $\widetilde{Re} \gtrsim 6$, slightly above the critical value for LSV formation and an inverse cascade; and a case in the G regime, with a robust inverse cascade possessing a strong peak at $k = 1$ driving energetically dominant LSVs. This figure illustrate how the pattern observed in figure 4(e,f) for fixed Pr and increasing $\widetilde{Ra}$ can be discerned for fixed $\widetilde{Ra}$ and decreasing Pr.

Following Guervilly *et al.* (2014), we can characterise the kinetic energy of the barotropic flow using the ratio of total kinetic energy to vertical kinetic energy,

$$\Gamma = K/(3K_z). \tag{3.2}$$

The factor of 3 in the denominator ensures that $\Gamma \to 1$ if the kinetic energy is equipartitioned between the horizontal and vertical components of the velocity. Conversely, when the barotropic kinetic energy dominates, we expect this ratio to become significantly larger than unity. Figures 6(a) and 6(b) show Γ for all of the simulations as a function of $\widetilde{Ra}$ and $\widetilde{Re}$, respectively. In agreement with the DNS calculations of Guervilly *et al.* (2014), $\Gamma \approx 1$ for small values of $\widetilde{Ra}$, then increases rapidly once LSVs begin to form. We find that Γ reaches a maximum of $\Gamma_{max} \approx 5.5$, that appears to be independent of the particular value of Pr, though only the $Pr = 1$ and $Pr = 1.5$ simulations show a maximum value. For $Pr = 1$, Γ reaches a maximum value at $\widetilde{Ra} = 80$,
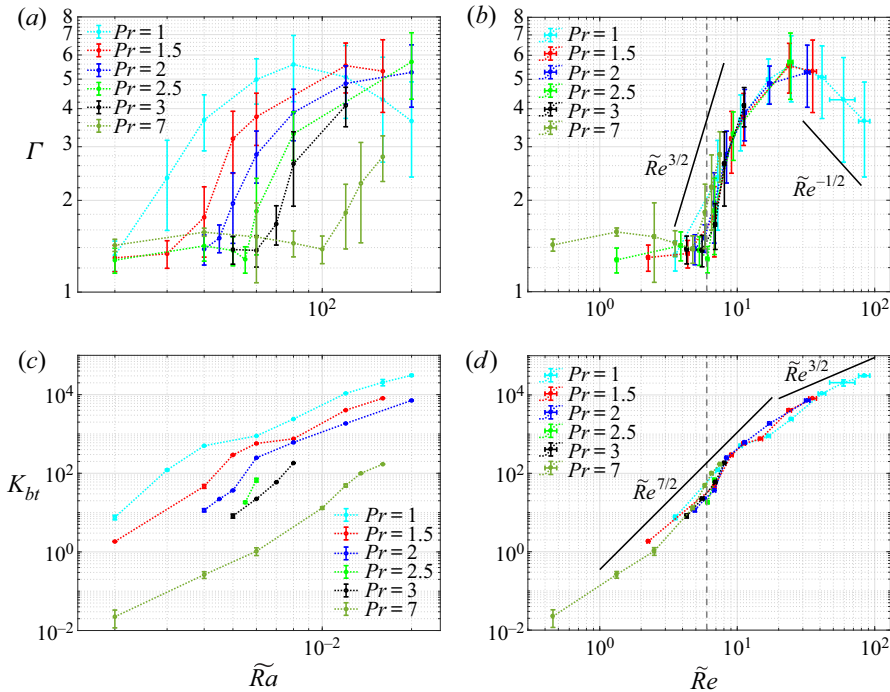
913 A18-16

Figure 6. Scaling behaviour of the kinetic energy for all of the simulations. (*a*) Ratio of the total kinetic energy to the vertical kinetic energy (Γ) versus $\widetilde{Ra}$; (*b*) Γ versus $\widetilde{Re}$; (*c*) barotropic kinetic energy K_{bt} versus $\widetilde{Ra}$; (*d*) K_{bt} versus $\widetilde{Re}$. The vertical dashed line at $\widetilde{Re} = 5.812$ in (*b,d*) demarcates the onset of LSV-dominant behaviour. Slopes in (*b,d*) are shown for reference.

whereas for $Pr = 1.5$, Γ_{max} occurs at $\widetilde{Ra} = 120$, suggesting that the value of $\widetilde{Ra}$ at which Γ_{max} is observed increases rapidly with Prandtl number.

Since the value of $\widetilde{Ra}$ at which LSVs begin to form is *Pr*-dependent, Γ is also plotted as a function of $\widetilde{Re}$ in figure 6(*b*). The data suggest that the evolution of Γ is uniquely determined by $\widetilde{Re}$ (or $(\widetilde{Ra} - \widetilde{Ra}_c)Pr^{-1}$ according to figure 1*b*) since all curves show self-similar behaviour, independent of the particular value of *Pr*. The dashed vertical line indicates $\widetilde{Re} = 5.812$, the lowest value at which the ($k = 1$) LSVs have been observed to become dominant. For cases in which $\widetilde{Re}$ is below this threshold value, Γ is close to 1 for all values of *Pr*, and the convective pattern, or flow regime, for all of these cases can be qualitatively classified as cellular or convective Taylor columns. Above this threshold value of the Reynolds number, we find both plumes and eventually geostrophic turbulence as $\widetilde{Re}$ grows. For both the $Pr = 1$ and $Pr = 1.5$ cases, Γ_{max} is reached for $\widetilde{Re} \simeq 24$.

We emphasise that since all of the calculations in the present work were carried out with the QG model, the observed decrease of Γ for large values $\widetilde{Ra}$ is not due to a loss of rotational constraint. Although the DNS study of Guervilly *et al.* (2014) also report a decrease in Γ for sufficiently large forcing, their observed decrease might be caused by an increase in the Rossby number with increasing forcing. In the present study, *Ro* remains asymptotically small, regardless of the thermal forcing. Also, as pointed out previously, the LSVs observed in Guervilly *et al.* (2014) are predominantly cyclonic, whereas the LSVs observed in the present simulations are dipolar.

Figures 6(*c*) and 6(*d*) show the barotropic kinetic energy versus $\widetilde{Ra}$ and $\widetilde{Re}$, respectively. In figure 6(*d*), slopes of $\widetilde{Re}^{7/2}$ and $\widetilde{Re}^{3/2}$ (found empirically) are shown as reference, along

with the vertical dashed line denoting the threshold Reynolds number $\widetilde{Re} = 5.812$. The 's-shaped' behaviour of the data, along with Γ, suggests that the barotropic mode is growing at an ever-decreasing rate as $\widetilde{Ra}$ is increased. Taking the barotropic kinetic energy K_{bt} scaling with $\widetilde{Re}$ as illustrated in figure 6(d) and with $K_{bc} \sim \widetilde{Re}^2$ (found empirically and consistent with the expectation $K_{bc} \sim K_z \sim \widetilde{Re}^2$; see supplementary figure 2), we can derive the expected evolution of Γ in the growing ($6 \lesssim \widetilde{Re} \lesssim 24$) and decaying ($\widetilde{Re} > 24$) regimes. In the former, under the assumption that $K_{bt} \gg K_{bc}, K_z$, we obtain $\Gamma \sim \widetilde{Re}^{3/2}$; in the latter, taking $\widetilde{Re} \to \infty$, we obtain $\Gamma \sim \widetilde{Re}^{-1/2}$. These slopes are illustrated in figure 6(b), for reference.

To better understand the change in scaling behaviour of the barotropic kinetic energy with increasing Rayleigh number, we examine the nonlinear convective forcing term in the barotropic vorticity equation (2.9). In particular, the nonlinear baroclinic term can be written as

$$\langle J[\psi', \zeta'] \rangle = \nabla_\perp \cdot \langle \boldsymbol{u}' \zeta' \rangle, \tag{3.3}$$

which suggests that the decreased efficiency of the barotropic mode is due to a drop in correlations between the baroclinic velocity and baroclinic vorticity. We calculated the cross-correlation coefficient for the x-component of the baroclinic velocity vector and baroclinic vorticity, defined as

$$C(u', \zeta') = \frac{\overline{\langle (\zeta' u')^2 \rangle}}{\sqrt{\langle (\zeta' \zeta')^2 \rangle \langle (u' u')^2 \rangle}}, \tag{3.4}$$

and analogously for the cross-correlation for the y-component of the baroclinic velocity field and the baroclinic vorticity, $C(v', \zeta')$. We note that this definition leads to $C = 0.5$ for perfect correlation between one component of the baroclinic velocity vector and the baroclinic vorticity, since the statistics are isotropic in the horizontal plane when sufficiently time averaged. The coefficients were computed over the entire investigated range of $\widetilde{Ra}$ for the case $Pr = 1$. Figure 7 shows the average value

$$C(\boldsymbol{u}', \zeta') = \frac{C(u', \zeta') + C(v', \zeta')}{2}. \tag{3.5}$$

The vertical dashed lines in the figure indicate the $\widetilde{Ra}$ values that correspond to the transition to LSV-forming regimes and to the maximum value of Γ. We observe that $C(\boldsymbol{u}', \zeta')$ decays as $\widetilde{Ra}$ is increased from $\widetilde{Ra} > 20$, suggesting one possible reason for the reduced rate of growth of the barotropic kinetic energy with increasing Rayleigh number. We also observe a change in slope as $\widetilde{Ra} > 80$ (the value for which Γ reaches the maximum value for $Pr = 1$), suggesting a complex interaction between the barotropic and baroclinic flows.

3.3. *The influence of initial conditions*

For the cases indicated by the superscript $*$ in table 1, additional simulations were carried out to test the influence of initial conditions on the occurrence of LSVs. In particular, for cases capable of forming LSVs ($\widetilde{Re} > 6$), we checked that the kinetic energy of the saturated state is independent of the presence of LSVs in the initial condition. Our results indicate that both baroclinic (or convective) amplitude (measured by $\widetilde{Re}$) and the barotropic
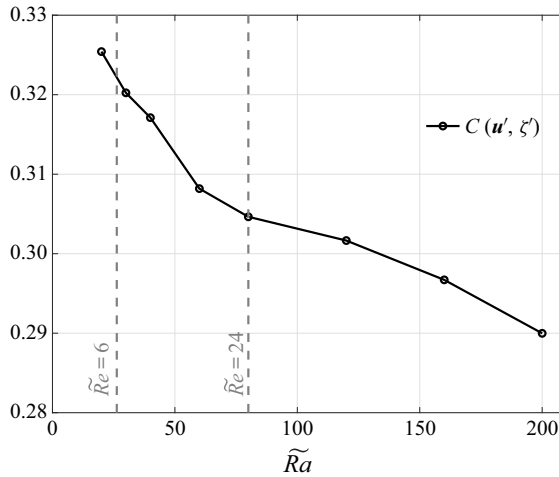
Figure 7. Correlation coefficient between the baroclinic vorticity and the horizontal components of the baroclinic velocity as a function of the Rayleigh number $\widetilde{Ra}$. The Prandtl number is fixed at $Pr = 1$. A value of $C = 0.5$ is perfect correlation for one component of the velocity vector. The vertical lines annotated with $\widetilde{Re} = 6$ and $\widetilde{Re} = 24$ indicate the approximate $\widetilde{Ra}$ values at which the flow becomes LSV dominant and convection dominant, respectively (see figure 6a).

kinetic energy in the saturated state do not depend on the initial condition, but only depend on Pr and $\widetilde{Ra}$. As an example, in figure 8 we show this by illustrating the time evolution of the kinetic energy per unit volume, $K(t)$, and the vertical Reynolds number, $\widetilde{Re}(t)$, for the case ($\widetilde{Ra} = 50$, $Pr = 1.5$). Two simulations were run for this case: one started from a random initial condition that does not contain pre-existing LSVs (labelled as 'random IC' in figure 8), and one started from an initial condition with LSVs already present in the domain, given from the saturated state of the ($\widetilde{Ra} = 40$, $Pr = 1$) case (labelled as 'LSVs IC'). In the former case, the initial growth of kinetic energy is due to the formation of the LSVs caused by the imbalance $T_k + F_k > |D_k|$ for $k = 1$. In the latter case, the LSVs initially present in the system were formed at a higher $\widetilde{Re}$ and due to a stronger inverse cascade than the one developed for ($\widetilde{Ra} = 50$, $Pr = 1.5$). Therefore, initially the imbalance $T_k + F_k < |D_k|$ leads to a kinetic energy decay as the LSVs cannot be energetically sustained. For both cases, a new state is eventually reached for which, statistically speaking $|D_k| = T_k + F_k$.

Similarly, we also found that for cases in which $\widetilde{Re} \lesssim 6$, LSVs would eventually decay if present in the initial conditions. This result is in apparent contrast with DNS calculations where a large-intensity, domain-scale cyclonic vortex appears to be long lived when injected in a convective system characterised by $Ro = O(1)$, in which large-scale structure would not spontaneously form (Favier *et al.* 2019). Note, however, that in Favier *et al.* (2019) the subcritical sustenance of a LSV is only obtained in regimes for which $\widetilde{Ra}$ is large enough for the dynamics to be in a transition regime between states that are rotationally constrained and regimes for which the geostrophic balance is no longer valid at leading order. In the asymptotic QG model employed here, the latter is unattainable by definition (see § 2) and the subcritical formation of LSVs cannot be investigated in the present study. For simulations with $Ro \ll 1$ and $\widetilde{Ra}$ smaller than the threshold value for LSV formation, Favier *et al.* (2019) found that the final state is independent of the initial condition, in line with our results.
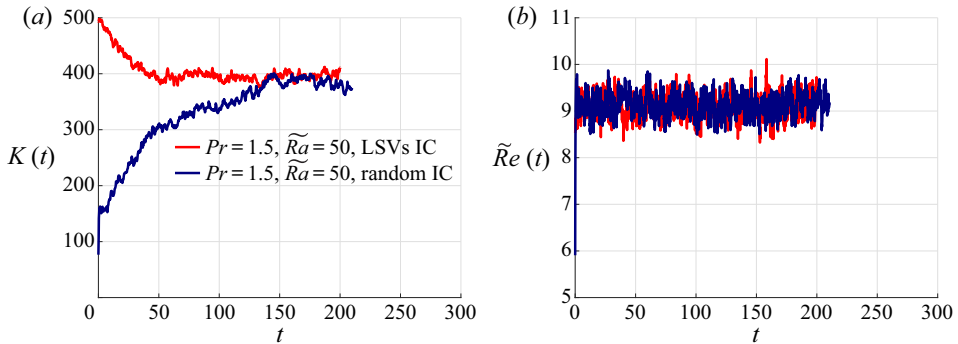
Figure 8. Influence of initial conditions on LSV formation. Kinetic energy (*a*) and reduced vertical Reynolds number (*b*) for the parameters $Pr = 1.5$ and $\widetilde{Ra} = 50$ from two different initial conditions: the case marked as 'random IC' has a random initial condition with no initial LSVs present; 'LSVs IC' marks an initial condition with well-developed LSVs in the system.

3.4. *The influence of box dimensions*

The horizontal dimensions of the simulation domain are represented in terms of integer multiples of the critical wavelength λ_c. We indicate the horizontal size of the computational domain by $n_c\lambda_c \times n_c\lambda_c$, with n_c being an integer. Most of the simulations were carried out with horizontal dimensions of $10\lambda_c \times 10\lambda_c$ (i.e. $n_c = 10$), which represents a trade-off between using a box size that is large enough to allow for computing converged statistics, and using a horizontal spatial resolution that is computationally feasible for an extensive exploration of the parameter space. Previous work has used values up to $n_c = 20$, but, to our knowledge, no systematic investigations of the box size on key quantities such as the Nusselt number and Reynolds number have been reported for rotating convection. For non-rotating convection, however, Stevens *et al.* (2018) showed that surprisingly large box dimensions are needed to obtain convergence in all statistical quantities; in contrast, the same authors found that globally averaged quantities such as the Nusselt number converged with relatively small box dimensions. For the present work we have carried out simulations for fixed Rayleigh number and Prandtl number of $\widetilde{Ra} = 40$ and $Pr = 1$. Robust LSVs are present with this parameter combination. Time series of these simulations are available in the supplementary material (see supplementary figure 1).

Figure 9 shows the convective Reynolds number and Nusselt number, and the barotropic and baroclinic kinetic energy for a range of box sizes. The solid lines in figure 9(*a*) show the Nusselt and Reynolds number for a simulation in which the barotropic mode was set to zero at each time step. We observe a nearly 23 % increase in the heat transport when the barotropic mode is not present. This result might be interpreted in terms of the horizontal mixing that is induced by the barotropic mode; the vertical transport of heat is reduced when horizontal motions sweep heat laterally. In addition, we find that the Reynolds number is reduced by ≈ 4.4 % with respect to the $n_c = 20$ case. This observation suggests that the inverse cascade plays a relatively small role in influencing the amplitude of the convective flow speeds.

An estimate for the intensity of LSVs based on the domain size can be made from the following simple argument. When well-developed LSVs are present, the dominant component of the kinetic energy spectra ($k \lesssim 5$) scales approximately as $K_{bt}(k^*) \sim k^{*-3}$ (Kraichnan 1967; Smith & Waleffe 1999; Rubio *et al.* 2014), where $k^* = k\tilde{k}_{box}$, with $\tilde{k}_{box} = 2\pi L_{box}^{-1}$ and $L_{box} = n_c\lambda_c$, is the dimensional box-scale wavenumber. Calculating the total
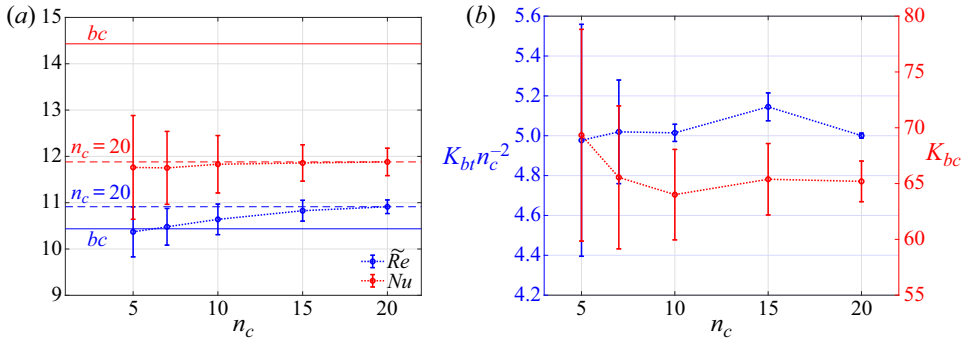
913 A18-20

Figure 9. Influence of the horizontal dimensions of the simulation domain on various quantities. Results for simulations with different horizontal dimensions, as characterised by $n_c\lambda_c \times n_c\lambda_c$, where n_c is an integer and λ_c is the critical horizontal wavelength. (a) Time-averaged Reynolds number $\widetilde{Re}$ and Nusselt number Nu versus n_c; (b) normalised barotropic kinetic energy $K_{bt}n_c^{-2}$ and baroclinic kinetic energy K_{bc}. For all simulations shown here $Pr = 1$ and $\widetilde{Ra} = 40$. The horizontal solid blue and red lines labelled 'bc' represent the average values of $\widetilde{Re}$ and Nu, respectively, calculated for a simulation with $n_c = 10$ in which the barotropic flow is set to zero. The horizontal dashed lines indicate the $n_c = 20$ values for comparison with the baroclinic case.

kinetic energy we obtain

$$K_{bt} = \int K_{bt}(k^*) \, \mathrm{d}k^* \sim k^{*-2} \sim L_{box}^2, \qquad (3.6)$$

where $K_{bt} \simeq K_{bt}(k^* = \tilde{k}_{box})$ when robust LSVs are observed in the system. In particular, by doubling the linear size of the (squared) domain the kinetic energy of LSVs is allowed to quadruple in magnitude. The DNS study of Favier *et al.* (2014) also observed an increase in the barotropic kinetic energy with increasing box size. Our QG data shown in figure 9(*b*) are supportive of this quadratic dependence on box size.

3.5. *Scaling laws for the baroclinic dynamics*

Here, we discuss least-squares fits to the baroclinic quantities $\widetilde{Re}$ and Nu. Power-law scalings were computed from all data collected in this study (see table 1 and figure 1*a*) for various subsets of $\widetilde{Ra}$ and Pr. For $\widetilde{Re}$ with varying Pr, we used power-law fits of the form

$$\widetilde{Re} = \alpha_r(\widetilde{Ra} - \widetilde{Ra}_c)^{\beta_r}Pr^{\gamma_r}, \qquad (3.7)$$

where α_r, β_r and γ_r are all numerically computed constants. For constant Pr, we used

$$\widetilde{Re} = \alpha_r(\widetilde{Ra} - \widetilde{Ra}_c)^{\beta_r}. \qquad (3.8)$$

The numerically computed constants are denoted by α_r, β_r and γ_r and given in table 2.

Fitting to all available data reported in this study (including the $Pr = 10$ dataset from Calkins *et al.* 2016) we obtain $(\alpha_r, \beta_r, \gamma_r) = (0.1883, 1.1512, -1.2172)$. We notice that these values are not too different from a linear scaling of the form $\widetilde{Re} \sim \widetilde{Ra}Pr^{-1}$, again suggesting that the reduced Grashof number plays a key role in controlling the dynamics. For many of the cases we find that β_r is closer to unity when a single value of Pr is used. Figure 10(*a*) shows the compensated Reynolds number $\widetilde{Re}Pr/\widetilde{Ra}$, where we see that there is a range of $\widetilde{Ra}$ values over which this scaling provides a reasonably good fit. However, significant departure from this linear Grashof number scaling is observed for

Pr	$\widetilde{Ra}$	α_r	β_r	γ_r
[1, 10]	[20, 200]	0.1883	1.1512	−1.2172
[1, 7]	[20, 200]	0.1899	1.1502	−1.2376
1	[20, 200]	0.1354	1.2198	—
1.5	[20, 160]	0.1567	1.0758	—
2	[20, 200]	0.1330	1.0399	—
2.5	[20, 200]	0.1375	0.9864	—
3	[20, 120]	0.1638	0.9007	—
7	[20, 160]	0.0522	0.9912	—
10	[20, 120]	0.0245	1.0792	—

Table 2. Least-squares fits to the Reynolds number, $\widetilde{Re} = \alpha_r (\widetilde{Ra} - \widetilde{Ra_c})^{\beta_r} Pr^{\gamma_r}$ (for data encompassing multiple Pr) or $\widetilde{Re} = \alpha_r (\widetilde{Ra} - \widetilde{Ra_c})^{\beta_r}$ (when a single Pr is considered).
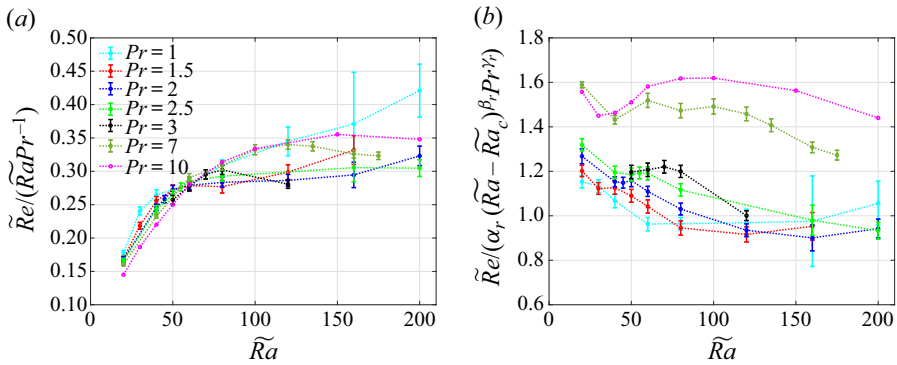
Figure 10. Scaling of the Reynolds number with $\widetilde{Ra}$. (a) Compensated $\widetilde{Re}$ calculated according to $\widetilde{Re} \sim \widetilde{Ra} Pr^{-1}$. (b) Compensated $\widetilde{Re}$ calculated according to the law (3.7) and with values of α_r, β_r and γ_r reported in table 2 for $Pr \in [1, 10]$ and $\widetilde{Ra} \in [20, 200]$ (i.e. all available $\widetilde{Re}$ data).

the lower values of Pr, i.e. those simulations that are characterised by the largest values of $\widetilde{Re}$. Interestingly, this departure seems to be correlated with the behaviour of the kinetic energy ratio Γ; the largest departures from the linear Grashof number scaling are observed for cases that possess the peak Γ_{max}, i.e. those cases in which $\widetilde{Re} \gtrsim 24$.

We note that because the QG model employed here is asymptotically reduced, the Ekman number does not appear explicitly in the governing equations. However, we can relate our small-scale Reynolds number to the large-scale Reynolds number typically employed in DNS studies by noting that the convective length scale and fluid depth are related by $\ell = HEk^{1/3}$. Thus,

$$\widetilde{Re} = \frac{\langle W_{rms} \rangle \ell}{\nu} = \left(\frac{\langle W_{rms} \rangle H}{\nu} \right) \left(\frac{\ell}{H} \right) = ReEk^{1/3}. \tag{3.9}$$

Substituting the definition of the reduced Rayleigh number into the linear scaling $\widetilde{Re} \sim \widetilde{Ra}/Pr$ we have

$$\widetilde{Re} \sim \frac{\widetilde{Ra}}{Pr} = \frac{RaEk^{4/3}}{Pr}. \tag{3.10}$$

Pr	$\widetilde{Ra}$	α_n	β_n	γ_n
[1, 7]	[20, 200]	0.2169	1.1791	0.0481
[1, 2]	[20, 200]	0.0993	1.3776	−0.5276
[1, 7]	$\widetilde{Ra}(\widetilde{Re} > 24)$	0.0231	1.6643	−0.5493
[1, 7]	$\widetilde{Ra}(1.5 < \widetilde{Re} < 24)$	0.3616	0.9899	0.3194
1	[20, 200]	0.0372	1.5725	—
1	[120, 200]	0.0194	1.6989	—
1.5	[20, 160]	0.1781	1.2011	—
2	[20, 200]	0.2196	1.1504	—
2.5	[20, 200]	0.3798	1.0402	—
3	[20, 120]	0.6799	0.9147	—
7	[20, 160]	0.6495	0.9957	—

Table 3. Least-squares fits to $Nu = \alpha_n(\widetilde{Ra} - \widetilde{Ra}_c)^{\beta_n}Pr^{\gamma_n}$ (for data encompassing multiple Pr) or $Nu = \alpha_n(\widetilde{Ra} - \widetilde{Ra}_c)^{\beta_n}$ (when a single value of Pr is considered). The third and fourth rows indicate calculations for the cases for which, respectively, $\widetilde{Re} > 24$ and $1.5 < \widetilde{Re} < 24$. For $\widetilde{Re} = 24$ the maximum value of Γ is reached (see figure 6b) and data points for which $\widetilde{Re} < 1.5$ are excluded as they exhibit transitional behaviour (see figure 11).

Upon dividing through by $Ek^{1/3}$ and using (3.9) we have the relationship

$$Re \sim \frac{RaEk}{Pr}. \tag{3.11}$$

The above scaling is consistent with the recent spherical convection study of Guervilly *et al.* (2019). However, we note that although the above large-scale Reynolds number scaling is diffusion free, the corresponding small-scale scaling is not.

Analogous least-squares fits to the Nusselt number (Nu) are given by

$$Nu = \alpha_n(\widetilde{Ra} - \widetilde{Ra}_c)^{\beta_n}Pr^{\gamma_n}, \tag{3.12}$$

or

$$Nu = \alpha_n(\widetilde{Ra} - \widetilde{Ra}_c)^{\beta_n}, \tag{3.13}$$

for fixed values of Prandtl number. Results for various subsets of the explored parameters space are given in table 3. Figure 11(b) shows the compensated Nu according to (3.12) using all available data from the present study. From table 3 we see that the same fit using only the $1 \leqslant Pr \leqslant 2$ cases suggests a fit that is roughly consistent with the ultimate scaling

$$Nu \sim \widetilde{Ra}^{3/2}Pr^{-1/2}, \tag{3.14}$$

in agreement with Julien *et al.* (2012b). Cases characterised by a lower $\widetilde{Re}$ (e.g. $Pr \geqslant 3$) lead to a lower value for the exponent β_n while using only the highest $\widetilde{Re}$ cases ($Pr = 1$, $\widetilde{Ra} \geqslant 120$) leads to a higher value of β_n. Compensated Nu values, based on the ultimate scaling (3.14), are illustrated in figure 11(a). This plot and the scaling coefficients reported in table 3 show the different scaling behaviours for cases characterised by values of $\widetilde{Re}$ below and above the value of $\widetilde{Re} = 24$ for which Γ reaches its maximum value (see figure 6b). The former exhibit a Nu scaling with $\widetilde{Ra}$ less steep than the ultimate scaling (3.14), while above the transition the $\widetilde{Ra}$ exponent is higher. We also notice that the exponent γ_n is, respectively, negative and positive, indicating a complex behaviour of Nu in the input parameters $\widetilde{Ra}$ and Pr.
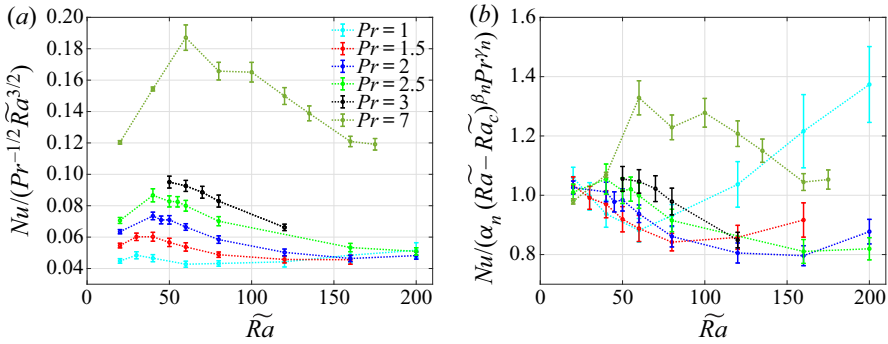
Figure 11. Scaling behaviour of the heat transport with $\widetilde{Ra}$. (a) Compensated Nu calculated according to $Nu \sim \widetilde{Ra}^{3/2}Pr^{-1/2}$. (b) Compensated Nu calculated according to the law (3.7), and with values of α_n, β_n and γ_n reported in table 3 for $Pr \in [1, 7]$ and $\widetilde{Ra} \in [20, 200]$ (i.e. all available Nu data).

3.6. *Balances*

Vertical profiles of the horizontal r.m.s. of each term present in the baroclinic vertical vorticity, vertical momentum and fluctuating heat equations are shown in figures 12(a), 12(b) and 12(c), respectively, for the most extreme calculation of $\widetilde{Ra} = 200$ and $Pr = 1$ ($\widetilde{Re} \approx 84$). All of the quantities shown have been time averaged. As shown previously (Julien *et al.* 2012b), within this high-$\widetilde{Ra}$ regime, the dominant terms in the governing equations are given by

$$\partial_t \zeta' + J[\psi, \zeta] - \langle J[\psi, \zeta] \rangle \approx 0, \tag{3.15}$$

$$\partial_t w + J[\psi, w] \approx 0, \tag{3.16}$$

$$\partial_t \theta + J[\psi, \theta] \approx 0, \tag{3.17}$$

which shows that horizontal advection of all these quantities is a key characteristic of this regime. Close inspection of the first of these balances reveals that, as $\widetilde{Re}$ grows, the advection of vorticity is increasingly dominated by the advection due to the barotropic flow, i.e. $J[\langle \psi \rangle, \zeta] \gg J[\psi', \zeta]$ for $\widetilde{Re} \gg 0$.

On their own, the 'balances' given above reveal little about the resulting dynamics. Higher-order, or subdominant, effects are necessary in the dynamics, especially with regard to heat transport. Figure 12(b) suggests that small differences between the r.m.s. values of $\partial_t w$ and $J[\psi, w]$ are necessary to balance the vertical pressure gradient, $\partial_Z \psi$. This perturbative effect repeats again at even higher order, as figure 12(b) shows that the buoyancy force and vertical viscous force are approximately balanced, i.e.

$$\frac{\widetilde{Ra}}{Pr}\vartheta \approx \nabla_\perp^2 w. \tag{3.18}$$

Moreover, we find a subdominant balance in the fluctuating heat equation between the advection of the mean temperature and horizontal thermal diffusion,

$$w\partial_Z \bar{\Theta} \approx \nabla_\perp^2 \theta. \tag{3.19}$$

To better understand the role of the subdominant balance between viscosity and buoyancy, we show in figure 13 the ratio of the vertical components of the r.m.s. viscous force, $F_{v,z} = \nabla_\perp^2 w$, to the r.m.s. buoyancy force, $F_{b,z} = \widetilde{Ra}Pr^{-1}\vartheta$, as a function $\widetilde{Re}$. All of the different Prandtl number cases appear to show qualitatively similar behaviour, and,
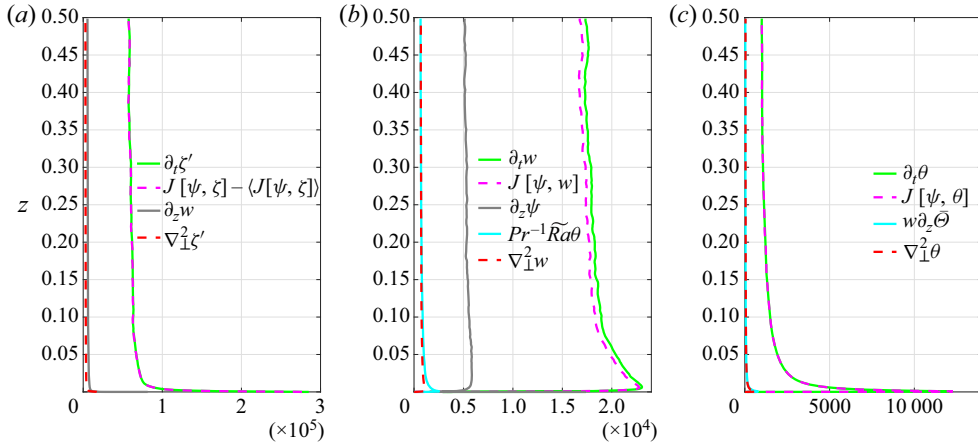
913 A18-24

Figure 12. Vertical profiles of r.m.s. terms in: (*a*) the baroclinic vorticity equation (obtained by subtracting (2.9) from (2.1)); (*b*) the vertical momentum equation (2.2); and (*c*) the fluctuating heat equation (2.3). Profiles have been calculated as temporal averages for the case $\widetilde{Ra} = 200$, $Pr = 1$ and are characteristic of all cases in the geostrophic turbulence regime, where LSV formation is robust.
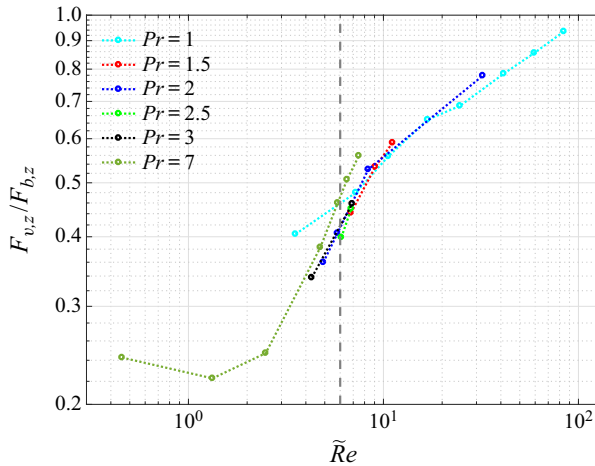

Figure 13. Ratio of the vertical components of the r.m.s. viscous force, $F_{v,z} = \nabla_\perp^2 w$, to the r.m.s. buoyancy force, $F_{b,z} = \widetilde{Ra}Pr^{-1}\vartheta$, as a function of $\widetilde{Re}$.

as figure 13 shows, a reasonable collapse of the data can be obtained when the force ratio is plotted versus the Reynolds number. Surprisingly, this ratio is an increasing function of $\widetilde{Re}$. This result is in stark contrast to non-rotating convection in which viscous forces become ever smaller (relative to other forces) with increasing Rayleigh number. Indeed, the so-called 'free-fall' scaling for convective flow speeds, characterised by a balance between buoyancy and inertia, relies on the influence of viscosity being weak (e.g. see Yan *et al.* 2019).

4. Discussion and conclusions

A systematic investigation of rapidly rotating convection was carried out to determine the necessary conditions under which large-scale vortices (LSVs) form, and how the

amplitude of such vortices and associated convective flow speeds scale with the input parameters. To achieve the extreme parameter regimes that are thought to be representative of natural systems such as planetary and stellar interiors, we have made use of an asymptotic description of the governing equations that rely on the assumption of a leading-order geostrophic balance. Varying the thermal Prandtl number has allowed us to determine the influence of fluid properties on the convective dynamics, and has also allowed for a more detailed control of the convective Reynolds numbers over our investigated range of Rayleigh numbers.

The LSVs form as a consequence of an inverse cascade that transports kinetic energy from small-scale, convective motions up to the system-wide scale, characterised by a box-normalised wavenumber of $k = 1$. These LSVs grow in time until the energy input from the convection is balanced by large-scale viscous dissipation. All of the simulations presented show evidence of this equilibration process, regardless of the particular values of Pr and $\widetilde{Ra}$. We find that LSV-dominant convection can be characterised by a critical convective Reynolds number $\widetilde{Re} \approx 6$ across the range of investigated Prandtl numbers, in satisfactory agreement with low-Ek DNS simulations performed at $Pr = 1$ (Favier *et al.* 2014; Guervilly *et al.* 2014). Although an increase in Pr leads to a concomitant increase in viscous dissipation for a fixed value of $\widetilde{Ra}$, we find, for the first time to our knowledge in the asymptotic regime of rapid rotation, evidence of LSV-dominant convection in the 'plume' regime. This finding is in agreement with DNS calculations presented in Guervilly *et al.* (2014), showing the presence of asymmetric LSVs for $Pr = 1$ for $\widetilde{Ra} \geqslant 20$. Whether the emergence of LSVs at lower $\widetilde{Ra}$ values is related to their asymmetric nature in finite Ro calculations will be the subject of future studies.

In particular we observed the formation of barotropic vortices with a Prandtl number as high as $Pr = 7$, a value that is representative of water at typical laboratory conditions. This finding suggests that LSVs may be detectable in laboratory experiments that use water as the working fluid. From the data reported in this study we can estimate a threshold value of $\widetilde{Ra}_t \simeq 120$ for the LSVs to form at $Pr = 7$ which can be translated into large-scale Ra_t for a given Ek via (2.5). State-of-the-art laboratory experiments can reach $Ek = 10^{-8}$ (Cheng *et al.* 2015, 2019) giving $Ra_t \simeq 5.6 \times 10^{12}$, a value for which heat transfer data suggest convection to be in a transitional regime between rotationally dominated and a non-rotating dynamics. We note that the presence of no-slip boundaries (not used in the present study) has been shown to partially suppress LSV formation (Plumley *et al.* 2016). By extension, we might expect rotating convection calculations in triply periodic domains, such as those used in the referenced turbulence studies (Smith & Waleffe 1999; Sen *et al.* 2012; Pouquet *et al.* 2013; Buzzicotti *et al.* 2018; Seshasayanan & Alexakis 2018) to facilitate the formation of vertically invariant, domain-filling vortices when compared to studies in the presence of horizontal boundaries. Note, however, that cases for which $K_{bt}(k = 1) > K_{bt}(k > 1)$ are found in presence of no-slip boundaries as well, suggesting that robust LSVs can be found in realistic settings. Indeed, recent DNS investigations (Guzmán *et al.* 2020) confirmed the formation of LSVs in presence of no-slip boundaries. In fact, heat transfer data show that the baroclinic dynamics is enhanced in presence of realistic boundary conditions (Stellmach *et al.* 2014; Plumley *et al.* 2016). Given these competing effects, additional studies are needed to determine the threshold for LSV-dominant convection with no-slip boundaries.

Several properties of LSVs have been studied. In agreement with the DNS study of Guervilly *et al.* (2014), we find that the relative size of the kinetic energy of the barotropic flow to that of the convection reaches a maximum value at a particular value of the

Rayleigh number. However, with DNS studies, there is a corresponding increase in the Rossby number with increasing Rayleigh number. In contrast, the asymptotic model used here only captures the asymptotically small Rossby number limit, showing that this change in the growth of the LSVs must be present in the rapidly rotating regime. When data from the entire range of Pr is plotted as a function of Reynolds number, the peak in the barotropic kinetic energy occurs near $\widetilde{Re} \approx 24$. Therefore, the growth of the barotropic kinetic energy slows as the Rayleigh number is increased, suggesting that there is an optimum forcing level. We find that this change in behaviour is related to a decrease in the velocity and vorticity correlations that are necessary to drive the inverse cascade. Our findings suggest that additional regimes, beyond the accessible limits of the present investigation, may be present in the convective dynamics as the Rayleigh number is increased further.

The horizontal dimensions of the simulation domain are shown to have a direct influence on the energy present in the LSVs. It is found that the energy associated with the LSVs grows quadratically with the horizontal dimension of the simulation domain (assuming domains of square cross-section), in agreement with DNS calculations (Favier *et al.* 2014). This finding is likely linked to the total available convective kinetic energy, which also grows quadratically with the horizontal dimensions of the simulation domain. Although a detailed investigation of the dynamical effect of this scaling was beyond the scope of the present investigation, this geometry-dependent effect may nevertheless have implications on the resulting dynamics.

The simulations suggest that there is no obvious scaling regime in the convective flow speeds with increasing Rayleigh number. A linear scaling of the form $\widetilde{Re} \sim \widetilde{Ra}/Pr$ appears to collapse the data over a limited range in $\widetilde{Ra}$, but the highest $\widetilde{Re}$ cases diverge from this scaling at the highest accessible values of $\widetilde{Ra}$. We note that this linear scaling can be translated to an equivalent large-scale Reynolds number scaling of the form $Re \sim EkRa/Pr$, which has been noted in previous studies of rotating convection (Guervilly *et al.* 2019). Although this scaling is independent of the diffusion coefficients ν and κ when viewed on the largest scales of the system, the small scales remain influenced by viscosity. Indeed, the simulations have revealed that the ratio of the r.m.s. viscous force to the r.m.s. buoyancy force in the vertical component of the momentum equation is an increasing function of $\widetilde{Ra}$ (or equivalently Ra). This observation may simply be a result of the energetics of the Boussinesq system that requires the net heat transport to be balanced by viscous dissipation. In this regard, it might be argued that viscosity is fundamental to rotating convective dynamics.

Author ORCIDs.

S. Maffei https://orcid.org/0000-0002-1603-4040;

K. Julien https://orcid.org/0000-0003-0718-7720;

M.A. Calkins https://orcid.org/0000-0002-6917-5365.

REFERENCES

ADAMS, M.M., STONE, D.R., ZIMMERMAN, D.S. & LATHROP, D.P. 2015 Liquid sodium models of the Earth's core. *Prog. Earth Planet. Sci.* **2** (1), 1–18.

AHLERS, G., GROSSMANN, S. & LOHSE, D. 2009 Heat transfer and large scale dynamics in turbulent Rayleigh–Bénard convection. *Rev. Mod. Phys.* **81** (2), 503–537.

AUBERT, J., BRITO, D., NATAF, H.-C., CARDIN, P. & MASSON, J.-P. 2001 A systematic experimental study of rapidly rotating spherical convection in water and liquid gallium. *Phys. Earth Planet. Inter.* **128**, 51–74.

AURNOU, J.M., BERTIN, V., GRANNAN, A.M., HORN, S. & VOGT, T. 2018 Rotating thermal convection in liquid gallium: multi-modal flow, absent steady columns. *J. Fluid Mech.* **846**, 846–876.

AURNOU, J.M., CALKINS, M.A., CHENG, J.S., JULIEN, K., KING, E.M., NIEVES, D., SODERLUND, K.M. & STELLMACH, S. 2015 Rotating convective turbulence in Earth and planetary cores. *Phys. Earth Planet. Inter.* **246**, 52–71.

AURNOU, J.M. & OLSON, P. 2001 Experiments on Rayleigh–Bénard convection, magnetoconvection, and rotating magnetoconvection in liquid gallium. *J. Fluid Mech.* **430**, 283–307.

BORUE, V. 1994 Inverse energy cascade in stationary two-dimensional homogeneous turbulence. *Phys. Rev. Lett.* **72** (10), 1475–1478.

BUZZICOTTI, M., ALUIE, H., BIFERALE, L. & LINKMANN, M. 2018 Energy transfer in turbulence under rotation. *Phys. Rev. Fluids* **3** (3), 034802.

CALKINS, M.A., HALE, K., JULIEN, K., NIEVES, D., DRIGGS, D. & MARTI, P. 2015 The asymptotic equivalence of fixed heat flux and fixed temperature thermal boundary conditions for rapidly rotating convection. *J. Fluid Mech.* **784**, R2.

CALKINS, M.A., JULIEN, K., TOBIAS, S.M., AURNOU, J.M. & MARTI, P. 2016 Convection-driven kinematic dynamos at low Rossby and magnetic Prandtl numbers: single mode solutions. *Phys. Rev. E* **93**, 023115.

CHAN, K.L. & MAYR, H.G. 2013 Numerical simulations of convectively generated vortices: application to the Jovian planets. *Earth Planet. Sci. Lett.* **371–372**, 212–219.

CHENG, J.S., MADONIA, M., GUZMÁN, A.J.A. & KUNNEN, R.P.J. 2019 Laboratory exploration of heat transfer regimes in rapidly rotating turbulent convection. arXiv:1911.04537.

CHENG, J.S., STELLMACH, S., RIBEIRO, A., GRANNAN, A., KING, E.M. & AURNOU, J.M. 2015 Laboratory-numerical models of rapidly rotating convection in planetary cores. *Geophys. J. Intl* **201**, 1–17.

CHERTKOV, M., CONNAUGHTON, C., KOLOKOLOV, I. & LEBEDEV, V. 2007 Dynamics of energy condensation in two-dimensional turbulence. *Phys. Rev. Lett.* **99** (8), 084501.

ECKE, R.E. & NIEMELA, J.J. 2014 Heat transport in the geostrophic regime of rotating Rayleigh–Bénard convection. *Phys. Rev. Lett.* **113**, 114301.

FAVIER, B., GUERVILLY, C. & KNOBLOCH, E. 2019 Subcritical turbulent condensate in rapidly rotating Rayleigh–Bénard convection. *J. Fluid Mech.* **864**, R1.

FAVIER, B., SILVERS, L.J. & PROCTOR, M.R.E. 2014 Inverse cascade and symmetry breaking in rapidly rotating Boussinesq convection. *Phys. Fluids* **26**, 096605.

FINLAY, C.C. & AMIT, H. 2011 On flow magnitude and field-flow alignment at Earth's core surface. *Geophys. J. Intl* **186**, 175–192.

GASTINE, T., WICHT, J. & AUBERT, J. 2016 Scaling regimes in spherical shell rotating convection. *J. Fluid Mech.* **808**, 690–732.

GASTINE, T., WICHT, J., DUARTE, L.D.V., HEIMPEL, M. & BECKER, A. 2014 Explaining Jupiter's magnetic field and equatorial jet dynamics. *Geophys. Res. Lett.* **41** (15), 5410–5419.

GUERVILLY, C., CARDIN, P. & SCHAEFFER, N. 2019 Turbulent convective length scale in planetary cores. *Nature* **570** (7761), 368–371.

GUERVILLY, C., HUGHES, D.W. & JONES, C.A. 2014 Large-scale vortices in rapidly rotating Rayleigh–Bénard convection. *J. Fluid Mech.* **758**, 407–435.

GUERVILLY, C., HUGHES, D.W. & JONES, C.A. 2015 Generation of magnetic fields by large-scale vortices in rotating convection. *Phys. Rev. E* **91**, 041001.

GUZMÁN, A.J.A., MADONIA, M., CHENG, J.S., OSTILLA-MÓNICO, R., CLERCX, H.J.H. & KUNNEN, R.P.J. 2020 Frictional boundary layer effect on vortex condensation in rotating turbulent convection. arXiv:2001.11889.

HAKIM, G.J., SNYDER, C. & MURAKI, D.J. 2002 A new surface model for cyclone–anticyclone asymmetry. *J. Atmos. Sci.* **59** (16), 2405–2420.

HEIMPEL, M., GASTINE, T. & WICHT, J. 2016 Simulation of deep-seated zonal jets and shallow vortices in gas giant atmospheres. *Nat. Geosci.* **9** (1), 19–23.

JONES, C.A. 2011 Planetary magnetic fields and fluid dynamos. *Annu. Rev. Fluid Mech.* **43**, 583–614.

JULIEN, K., AURNOU, J.M., CALKINS, M.A., KNOBLOCH, E., MARTI, P., STELLMACH, S. & VASIL, G.M. 2016 A nonlinear model for rotationally constrained convection with Ekman pumping. *J. Fluid Mech.* **798**, 50–87.

JULIEN, K., KNOBLOCH, E., MILLIFF, R. & WERNE, J. 2006 Generalized quasi-geostrophy for spatially anistropic rotationally constrained flows. *J. Fluid Mech.* **555**, 233–274.

JULIEN, K., KNOBLOCH, E., RUBIO, A.M. & VASIL, G.M. 2012a Heat transport in low-Rossby-number Rayleigh–Bénard convection. *Phys. Rev. Lett.* **109**, 254503.

JULIEN, K., KNOBLOCH, E. & WERNE, J. 1998 A new class of equations for rotationally constrained flows. *Theor. Comput. Fluid Dyn.* **11**, 251–261.

JULIEN, K., RUBIO, A.M., GROOMS, I. & KNOBLOCH, E. 2012b Statistical and physical balances in low Rossby number Rayleigh–Bénard convection. *Geophys. Astrophys. Fluid Dyn.* **106** (4–5), 392–428.

KING, E.M. & AURNOU, J.M. 2013 Turbulent convection in liquid metal with and without rotation. *Proc. Natl Acad. Sci.* **110** (17), 6688–6693.

KING, E.M., STELLMACH, S. & AURNOU, J.M. 2012 Heat transfer by rapidly rotating Rayleigh–Bénard convection. *J. Fluid Mech.* **691**, 568–582.

KING, E.M., STELLMACH, S., NOIR, J., HANSEN, U. & AURNOU, J.M. 2009 Boundary layer control of rotating convection systems. *Nature* **457**, 301–304.

KRAICHNAN, R.H. 1967 Inertial ranges in two-dimensional turbulence. *Phys. Fluids* **10** (7), 1417–1423.

KUNNEN, R.P.J., GEURTS, B.J. & CLERCX, H.J.H. 2010 Experimental and numerical investigation of turbulent convection in a rotating cylinder. *J. Fluid Mech.* **642**, 445–476.

LAURIE, J., BOFFETTA, G., FALKOVICH, G., KOLOKOLOV, I. & LEBEDEV, V. 2014 Universal profile of the vortex condensate in two-dimensional turbulence. *Phys. Rev. Lett.* **113** (25), 254503.

MAFFEI, S., CALKINS, M.A., JULIEN, K. & MARTI, P. 2019 Magnetic quenching of the inverse cascade in rapidly rotating convective turbulence. *Phys. Rev. Fluids* **4** (4), 041801.

MARTI, P., CALKINS, M.A. & JULIEN, K. 2016 A computationally efficent spectral method for modeling core dynamics. *Geochem. Geophys. Geosyst.* **17** (8), 3031–3053.

NIEMELA, J.J., BABUIN, S. & SREENIVASAN, K.R. 2010 Turbulent rotating convection at high Rayleigh and Taylor numbers. *J. Fluid Mech.* **649**, 509–522.

NIEVES, D., RUBIO, A.M. & JULIEN, K. 2014 Statistical classification of flow morphology in rapidly rotating Rayleigh–Bénard convection. *Phys. Fluids* **26** (8), 086602.

ORVEDAHL, R.J., CALKINS, M.A., FEATHERSTONE, N.A. & HINDMAN, B.W. 2018 Prandtl-number effects in high-Rayleigh-number spherical convection. *Astrophys. J.* **856** (1), 13.

OSSENDRIJVER, M. 2003 The solar dynamo. *Astron. Astrophys. Rev.* **11** (4), 287–367.

PLUMLEY, M., CALKINS, M.A., JULIEN, K. & TOBIAS, S.M. 2018 Self-consistent single mode investigations of the quasi-geostrophic convection-driven dynamo model. *J. Plasma Phys.* **84** (4), 735840406.

PLUMLEY, M. & JULIEN, K. 2019 Scaling laws in Rayleigh–Benard convection. *Earth Space Sci.* **6** (9), 1580–1592.

PLUMLEY, M., JULIEN, K., MARTI, P. & STELLMACH, S. 2016 The effects of ekman pumping on quasi-geostrophic Rayleigh–Bénard convection. *J. Fluid Mech.* **803**, 51–71.

POUQUET, A., SEN, A., ROSENBERG, D., MININNI, P.D. & BAERENZUNG, J. 2013 Inverse cascades in turbulence and the case of rotating flows. *Phys. Scr.* **2013** (T155), 014032.

POZZO, M., DAVIES, C.J., GUBBINS, D. & ALFÉ, D. 2013 Transport properties for liquid silicon-oxygen-iron mixtures at Earth's core conditions. *Phys. Rev.* B **87**, 014110.

RUBIO, A.M., JULIEN, K., KNOBLOCH, E. & WEISS, J.B. 2014 Upscale energy transfer in three-dimensional rapidly rotating turbulent convection. *Phys. Rev. Lett.* **112** (14), 144501.

RUTTER, M.D., SECCO, R.A., UCHIDA, T., LIU, H., WANG, Y., RIVERS, M.L. & SUTTON, S.R. 2002 Towards evaluating the viscosity of the Earth's outer core: an experimental high pressure study of liquid Fe-S (8.5 wt.% S). *Geophys. Res. Lett.* **29** (8), 58.

SEN, A., MININNI, P.D., ROSENBERG, D. & POUQUET, A. 2012 Anisotropy and nonuniversality in scaling laws of the large-scale energy spectrum in rotating turbulence. *Phys. Rev.* E **86** (3), 036319.

SESHASAYANAN, K. & ALEXAKIS, A. 2018 Condensates in rotating turbulent flows. *J. Fluid Mech.* **841**, 434–462.

SMITH, L.M. & WALEFFE, F. 1999 Transfer of energy to two-dimensional large scales in forced, rotating three-dimensional turbulence. *Phys. Fluids* **11** (6), 1608–1622.

SMITH, L.M. & YAKHOT, V. 1993 Bose condensation and small-scale structure generation in a random force driven 2D turbulence. *Phys. Rev. Lett.* **71** (3), 352–355.

SMITH, L.M. & YAKHOT, V. 1994 Finite-size effects in forced two-dimensional turbulence. *J. Fluid Mech.* **274**, 115–138.

SPALART, P.R., MOSER, R.D. & ROGERS, M.M. 1991 Spectral methods for the Navier–Stokes equations with one infinite and two periodic directions. *J. Comput. Phys.* **96**, 297–324.

SPRAGUE, M., JULIEN, K., KNOBLOCH, E. & WERNE, J. 2006 Numerical simulation of an asymptotically reduced system for rotationally constrained convection. *J. Fluid Mech.* **551**, 141–174.

STELLMACH, S., LISCHPER, M., JULIEN, K., VASIL, G., CHENG, J.S., RIBEIRO, A., KING, E.M. & AURNOU, J.M. 2014 Approaching the asymptotic regime of rapidly rotating convection: boundary layers versus interior dynamics. *Phys. Rev. Lett.* **113**, 254501.

STEVENS, R.J.A.M., BLASS, A., ZHU, X., VERZICCO, R. & LOHSE, D. 2018 Turbulent thermal superstructures in Rayleigh–Bénard convection. *Phys. Rev. Fluids* **3** (4), 041501.

STEWARTSON, K. & CHENG, H.K. 1979 On the structure of inertial waves produced by an obstacle in a deep, rotating container. *J. Fluid Mech.* **91**, 415–432.

SUMITA, I. & OLSON, P. 2002 Rotating thermal convection experiments in a hemispherical shell with hetergenous boundary heat flux: implications for the Earth's core. *J. Geophys. Res.* **107** (B8), ETG 5-1–ETG 5-18.

VOGT, T., HORN, S., GRANNAN, A.M. & AURNOU, J.M. 2018 Jump rope vortex in liquid metal convection. *Proc. Natl Acad. Sci. USA* **115** (50), 12674–12679.

VOROBIEFF, P. & ECKE, R.E. 2002 Turbulent rotating convection: an experimental study. *J. Fluid Mech.* **458**, 191–218.

DE WIJS, G.A., KRESSE, G., VOČADLO, L., DOBSON, D., ALFE, D., GILLAN, M.J. & PRICE, G.D. 1998 The viscosity of liquid iron at the physical conditions of the Earth's core. *Nature* **392** (6678), 805–807.

YAN, M., CALKINS, M.A., MAFFEI, S., JULIEN, K., TOBIAS, S.M. & MARTI, P. 2019 Heat transfer and flow regimes in quasi-static magnetoconvection with a vertical magnetic field. *J. Fluid Mech.* **877**, 1186–1206.

ZIMMERMAN, D.S., TRIANA, S.A., NATAF, H.-C. & LATHROP, D.P. 2014 A turbulent, high magnetic Reynolds number experimental model of Earth's core. *J. Geophys. Res.: Solid Earth* **119** (6), 4538–4557.